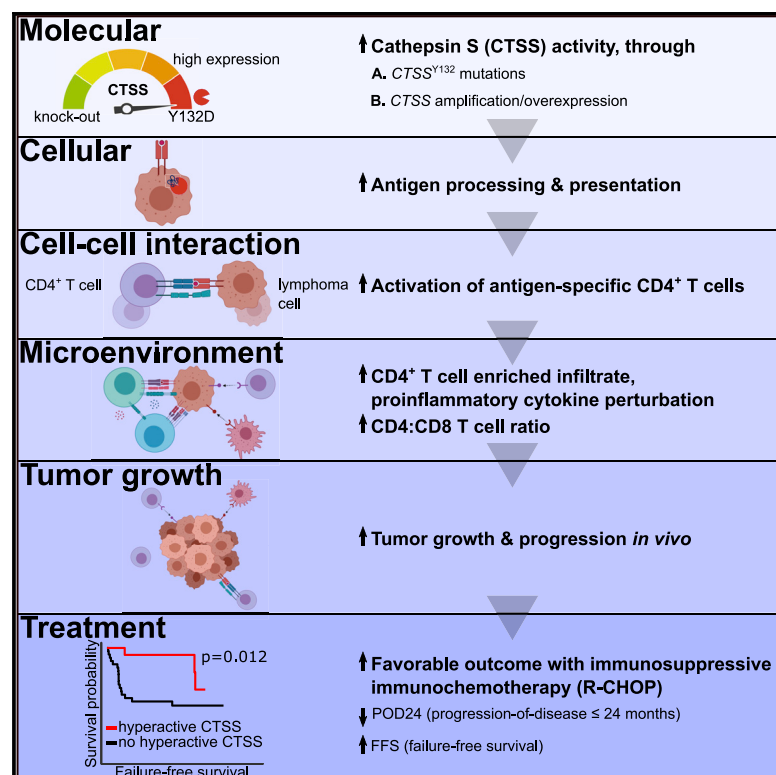


Cathepsin S Alterations Induce a Tumor-Promoting Immune Microenvironment in Follicular Lymphoma

Graphical Abstract



Authors

Deepak Bararia, Johannes A. Hildebrand, Sebastian Stolz, ..., Verena Passerini, Josef Mautner, Oliver Weigert

Correspondence

oliver.weigert@med.uni-muenchen.de

In Brief

Bararia et al. discover and functionally characterize a clinically relevant mechanism of tumor and immune cell interaction in follicular lymphoma, a prototypical type of blood cancer. *Cathepsin S* alterations result in aberrant hyperactivity of this lysosomal cysteine protease and induce a tumor-promoting CD4⁺ T cell enriched immune microenvironment.

Highlights

- CTSS hyperactivity through mutations or overexpression in ~20% of FL
- CTSS mutations cluster at Y132 and accelerate autocatalytic cleavage and activation
- CTSS hyperactivity increases CD4⁺ T cell activation and accelerates tumor growth *in vivo*
- Higher activity of immunosuppressive immunochemotherapy in CTSS-hyperactive human FL



Article

Cathepsin S Alterations Induce a Tumor-Promoting Immune Microenvironment in Follicular Lymphoma

Deepak Bararia,^{1,2,3,19} Johannes A. Hildebrand,^{1,2,3,19} Sebastian Stolz,¹ Sarah Haebe,¹ Stefan Alig,¹ Christopher P. Trevisani,¹² Francisco Osorio-Barrios,¹³ Michael D. Bartoschek,⁴ Michael Mentz,¹ Alessandro Pastore,⁵ Erik Gaitzsch,^{1,2,3} Michael Heide,^{1,2,3} Vindi Jurinovic,^{1,6} Katharina Rautter,¹⁸ Jay Gunawardana,¹⁶ Muhammed B. Sabdia,¹⁶ Monika Szczepanowski,⁷ Julia Richter,⁷ Wolfram Klapper,⁷ Abner Louissaint, Jr.,⁸ Christina Ludwig,⁹ Sebastian Bultmann,⁴ Heinrich Leonhardt,⁴ Sebastian Eustermann,^{10,21} Karl-Peter Hopfner,¹⁰ Wolfgang Hiddemann,^{1,2,3} Michael von Bergwelt-Baildon,^{1,2,3} Christian Steidl,¹¹ Robert Kridel,^{11,20} Joshua W.D. Tobin,¹⁶ Maher K. Gandhi,¹⁶ David M. Weinstock,¹² Marc Schmidt-Supprian,^{2,13} Menyhárt B. Sárosi,¹⁴ Martina Rudelius,¹⁷ Verena Passerini,^{1,2,3} Josef Mautner,¹⁵ and Oliver Weigert^{1,2,3,22,*}

¹Department of Medicine III, Laboratory for Experimental Leukemia and Lymphoma Research (ELLF), Hospital of the Ludwig-Maximilians-University (LMU), Munich, Bavaria 81377, Germany

²German Cancer Consortium (DKTK), Munich, Bavaria 81377, Germany

³German Cancer Research Center (DKFZ), Heidelberg, Baden-Wuerttemberg 69120, Germany

⁴Department of Biology II, Center for Integrated Protein Science Munich (CIPSM), Ludwig-Maximilians-University (LMU), Munich, Bavaria 81377, Germany

⁵Memorial Sloan Kettering Cancer Center, New York, NY 10065, USA

⁶Institute for Medical Information Processing, Biometry, and Epidemiology, Munich, Bavaria 81377, Germany

⁷Hematopathology Section, University Hospital Schleswig-Holstein, Campus Kiel, Kiel, Schleswig-Holstein 24105, Germany

⁸Massachusetts General Hospital, Department of Pathology, Boston, MA 02114, USA

⁹Bavarian Center for Biomolecular Mass Spectrometry (BayBioMS), Technical University of Munich, Munich, Bavaria 85354, Germany

¹⁰Gene Center, Ludwig-Maximilians-University, Munich, Bavaria 81377, Germany

¹¹Center for Lymphoid Cancer, British Columbia Cancer, Vancouver, BC V5Z 1L3, Canada

¹²Department of Medical Oncology, Dana-Farber Cancer Institute, Boston, MA 02215, USA

¹³Institute of Experimental Hematology, TranslaTUM, Klinikum rechts der Isar, Technical University of Munich, Munich, Bavaria 81675, Germany

¹⁴Institute of Inorganic Chemistry, Faculty of Chemistry and Mineralogy, Leipzig University, Leipzig, Saxony 04103, Germany

¹⁵Helmholtz Zentrum München & Technical University of Munich, Munich, Bavaria 81377, Germany

¹⁶Blood Cancer Research Group, Mater Research, University of Queensland, Translational Research Institute, Brisbane, QLD 4101, Australia

¹⁷Institute of Pathology, Ludwig-Maximilians-University (LMU), Munich, Bavaria 80337, Germany

¹⁸Immunoanalytics: Research Group Tissue Control of Immunocytes & Core Facility, German Research Center for Environmental Health, Helmholtz Zentrum München, Munich, Bavaria 81377, Germany

¹⁹These authors contributed equally

²⁰Present address: Princess Margaret Cancer Centre, UHN, Toronto, ON M5G 2M9, Canada

²¹Present address: European Molecular Biology Laboratory (EMBL), Heidelberg, Baden-Wuerttemberg 69117, Germany

²²Lead Contact

*Correspondence: oliver.weigert@med.uni-muenchen.de
<https://doi.org/10.1016/j.celrep.2020.107522>

SUMMARY

Tumor cells orchestrate their microenvironment. Here, we provide biochemical, structural, functional, and clinical evidence that *Cathepsin S* (CTSS) alterations induce a tumor-promoting immune microenvironment in follicular lymphoma (FL). We found CTSS mutations at Y132 in 6% of FL (19/305). Another 13% (37/286) had CTSS amplification, which was associated with higher CTSS expression. CTSS Y132 mutations lead to accelerated autocatalytic conversion from an enzymatically inactive proform to active CTSS and increased substrate cleavage, including CD74, which regulates major histocompatibility complex class II (MHC class II)-restricted antigen presentation. Lymphoma cells with hyperactive CTSS more efficiently activated antigen-specific CD4⁺ T cells *in vitro*. Tumors with hyperactive CTSS showed increased CD4⁺ T cell infiltration and proinflammatory cytokine perturbation in a mouse model and in human FLs. In mice, this CTSS-induced immune microenvironment promoted tumor growth. Clinically, patients with CTSS-hyperactive FL had better treatment outcomes with standard immunochemotherapies, indicating that these immunosuppressive regimens target both the lymphoma cells and the tumor-promoting immune microenvironment.



INTRODUCTION

Recent efforts have focused on dissecting the molecular aberrations within cancer cells, but it is increasingly recognized that tumor cells also orchestrate and depend on interactions with non-malignant cells of the tumor microenvironment. The immune microenvironment imposes profound constraints upon tumor development (Binnewies et al., 2018). At the same time, tumor cells can induce their own advantageous growth environment. Follicular lymphoma (FL) typifies the clinical implications of this evolving paradigm (Scott and Gascoyne, 2014).

FL is among the most common lymphoma worldwide (Swerdlow et al., 2016). Most patients present with advanced-stage disease and are still considered incurable. The molecular hallmark of FL is chromosomal rearrangement and overexpression of anti-apoptotic BCL2. Additional recurrent gene mutations are common in FL, many of which are likely to have distinct impact on the biology and the clinical course of the disease (O'Shea et al., 2008; Pastore et al., 2015; Weigert and Weinstock, 2017). In addition to cell intrinsic alterations, however, immune cells and signals from the immune microenvironment have also been shown to be significantly associated with treatment outcome (Dave et al., 2004; Glas et al., 2007; Huet et al., 2018; Kiaii et al., 2013).

Recent studies have provided first insights into how genetic alterations modulate the complex crosstalk between lymphoma cells and other immune cells. For example, mutations in *CREBBP* (Green et al., 2015; Jiang et al., 2017; Zhang et al., 2017), *B2M* (Challa-Malladi et al., 2011), and *EZH2* (Ennishi et al., 2019) are highly recurrent in FL and suppress the expression of major histocompatibility complex class II (MHC class II) and class I, thereby promoting immune escape. Also, loss of *TNFRSF14* (also known as HVEM) by mutations and/or deletions promote lymphomagenesis by various cell-intrinsic and cell-extrinsic mechanisms, including increased recruitment of CD4⁺ T follicular helper (T_{FH}) cells (Boice et al., 2016), thereby fostering a supportive microenvironment.

We have previously identified *Cathepsin S* (CTSS) to be recurrently and significantly mutated in FL (Pastore et al., 2015). CTSS encodes for a cysteine protease that is highly expressed in endolysosomes of antigen-presenting cells (APCs) and malignant B cells. In APCs, CTSS is involved in proteolytical processing of antigenic peptides for presentation on MHC class II to be recognized by antigen-specific CD4⁺ T cells (Riese et al., 1996). Furthermore, CTSS cleaves CD74 (invariant chain or Ii) to release CLIP (class II invariant chain peptide), which shields the MHC class II peptide-binding groove against premature peptide binding (Rückrich et al., 2006).

In cancer, cathepsins have been mostly studied with respect to their role as secreted proteases involved in the turnover and degradation of the extracellular matrix (Olson and Joyce, 2015). Overexpression of CTSS has been linked to tumor progression, invasion, and metastasis and is frequently associated with poor prognosis in solid cancers (Sevenich et al., 2014).

Here, we provide biochemical, structural, functional, and clinical evidence that aberrant hyperactivation of CTSS in lymphoma cells leads to more efficient activation of antigen-specific CD4⁺ T cells, eliciting a tumor-promoting immune response within the microenvironment.

RESULTS

CTSS Mutations Cluster at Y132

We sequenced tumor biopsy specimens from patients with advanced FL from Germany and Canada by using a customized target-capture bait set that included full-length CTSS (Pastore et al., 2015). Among 305 cases, we found mutations of CTSS in 8% of FL (23/305) and the majority clustered at Y132 (19/23) (Figure 1A), converting Y (TAT) to D (GAT) (16/19). We validated and confirmed CTSS Y132D mutations to be somatic by Sanger sequencing (Figure 1B). We corrected CTSS variant allele frequencies (VAFs) by cancer cell fractions (CCFs), which could be calculated from available whole-genome copy number (CN) data for 12 of 19 CTSS mutated cases. This analysis showed that 5 mutations were clonal (42%) and 7 mutations were subclonal (58%), the latter all consisting of Y132D (Figure 1C). Overall, this indicates that CTSS mutations are recurrent, cluster at the mutational hotspot Y132, and can be subclonal.

Moreover, we identified convergent evolution of CTSS mutations at Y132 in a case of donor-derived FLs (Figure 1D). Specifically, following an allogeneic bone marrow transplantation (BMT), both the donor and the recipient developed FLs, which evolved from a common precursor clone, as demonstrated by the presence of identical somatic alterations, including the FL hallmark translocation t(14;18) (Weigert et al., 2012). Both FLs harbored CTSS mutations that affected Y132; however, these mutations were not identical (Figures 1D and 1E). Again, these CTSS mutations had lower VAFs (0.18 and 0.08 for Y132N in the donor's and Y132S in the recipient's FL, respectively) and were not detected by previous whole-exome sequencing (Weigert et al., 2012). Overall, this case illustrates that these CTSS mutations were independently acquired in later branches during the clonal evolution of each FL, with a remarkable selection pressure toward mutations at Y132.

CTSS Y132 Mutants Have Increased Proteolytic Activity

Positive selection for hotspot mutations suggests a gain-of-function. CTSS is synthesized as an enzymatically inactive proenzyme of 331 amino acids (aa), consisting of an N-terminal 16-aa signal peptide (SP) that is removed during the passage to the endoplasmic reticulum (ER) an autoinhibitory propeptide that is involved in the proper protein folding and targeting to the endolysosomes, and proteolytically active mature CTSS (Figure 1A).

We used CRISPR-Cas9 to introduce the Y132D mutation into the endogenous CTSS locus of Karpas422 (Figure S1A), a human B-cell lymphoma cell line that is wild type (WT) for CTSS and harbors the FL hallmark translocation t(14;18). Single-cell-derived Y132D mutant clones (#E2 and #H41) consistently showed increased ratios of mature CTSS (24 kD) to pro-CTSS (36 kD) by western blot (Figure 2A, left). Protein quantification by densitometry revealed higher levels of mature CTSS in Y132D than in WT cells (Figure 2A, right). The increased protein levels of mature CTSS in Y132 mutant cells could not be attributed to differences in CTSS mRNA levels, as demonstrated by quantitative reverse-transcription PCR (Figure S2A). As a control, we used CRISPR-Cas9 to generate a single-cell-derived CTSS knockout (CTSS^{KO}) clones from Karpas422 and DG75

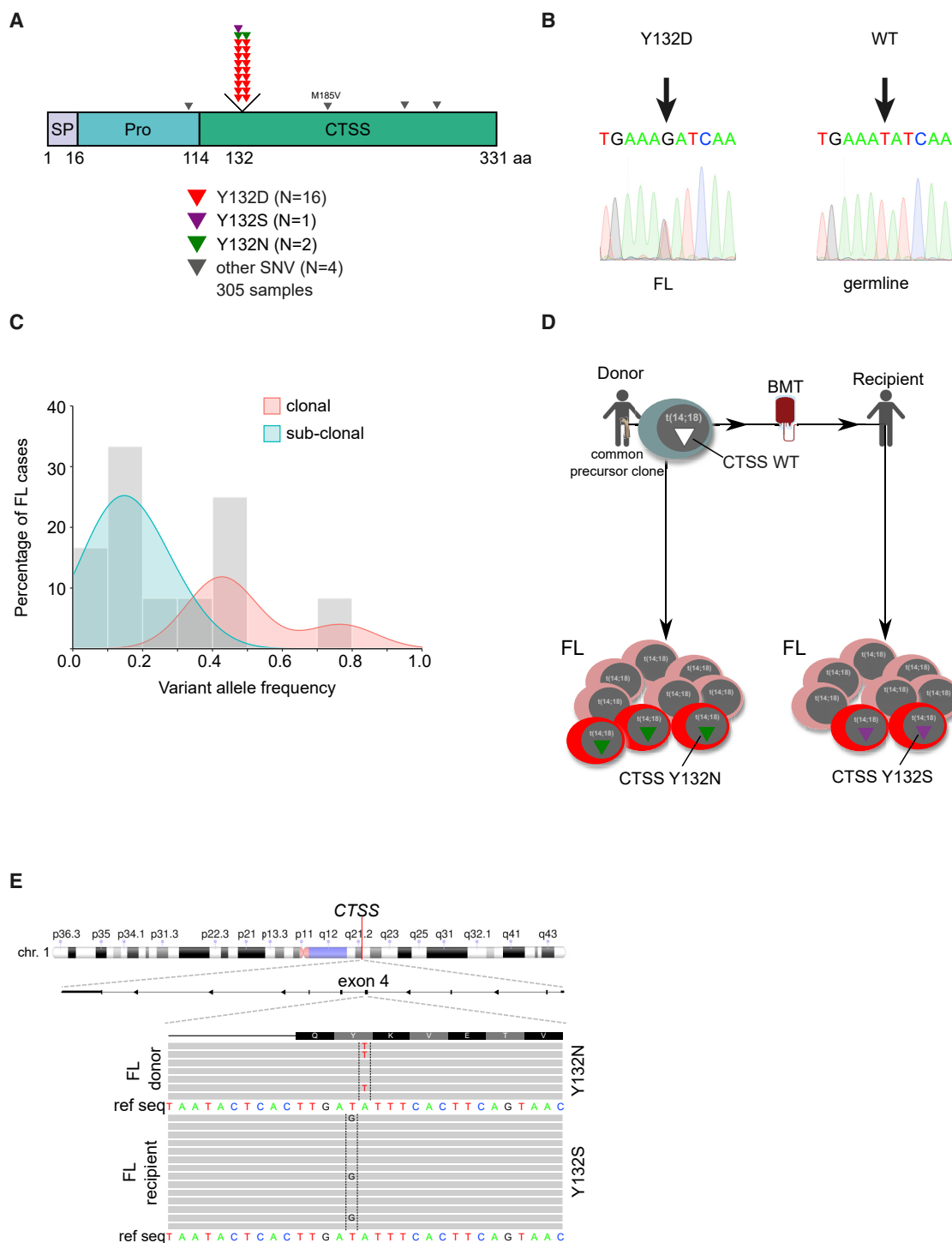


Figure 1. CTSS Mutations Are Recurrent in FL and Cluster at the Mutational Hotspot Y132

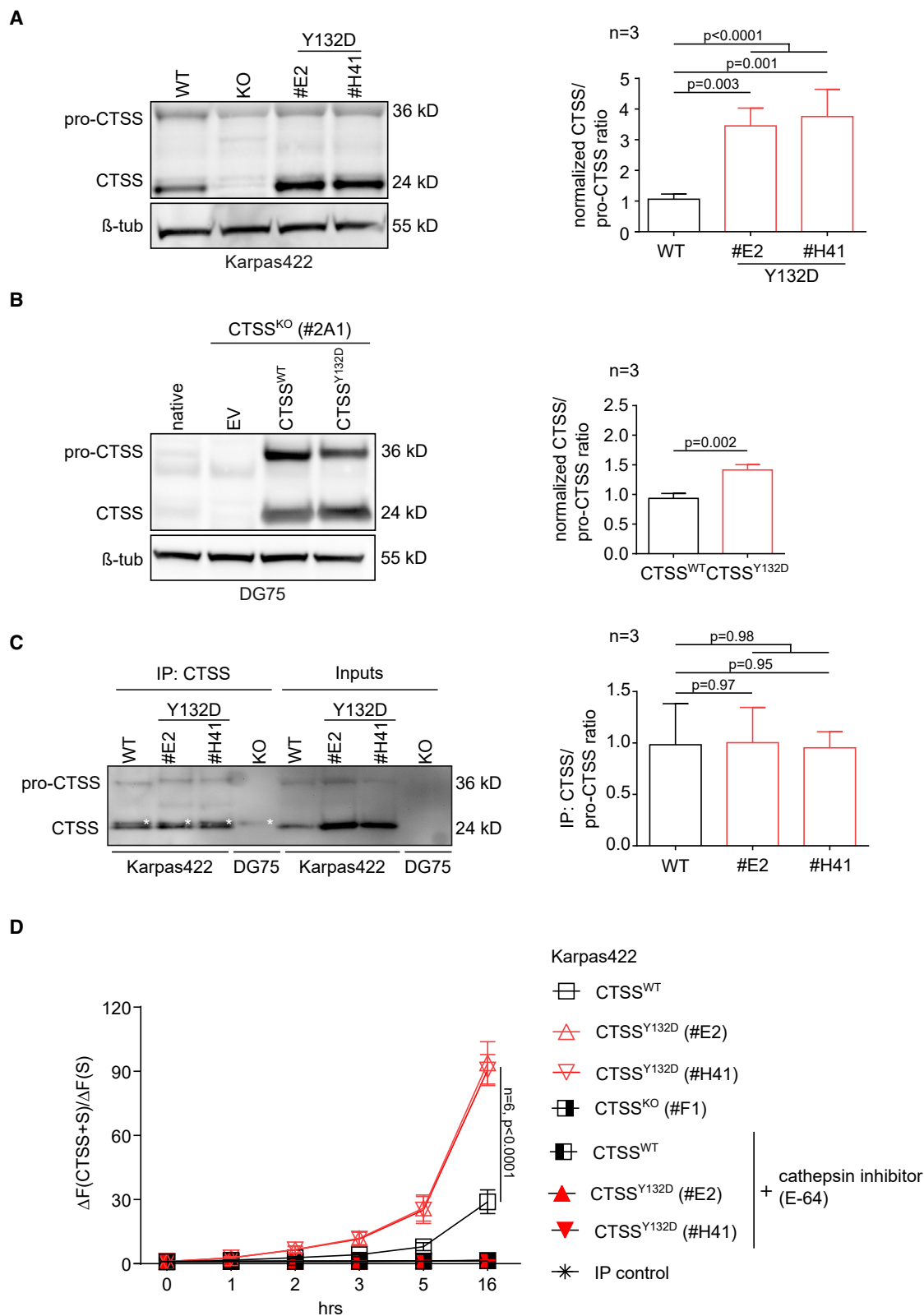
(A) Distribution and frequency of CTSS mutations from a cohort of 305 FL from a previously reported cohort (Pastore et al., 2015). Schematic structure of CTSS showing the signal peptide (SP), propeptide (Pro), and the mature CTSS domains; aa, amino acid. See also Table S3 for sequencing details.

(B) Sanger sequencing of a primary FL sample (FL55_03303) harboring a somatic CTSS Y132D mutation.

(C) Cancer cell fraction (CCF)-corrected variant allele frequencies (VAFs) of CTSS Y132 mutations. CCFs were available for 12 of 19 FL with CTSS Y132 mutations.

(D) Schematic of a case of donor-derived FL following an allogeneic bone marrow transplantation (BMT).

(E) Targeted DNA sequencing reads showing distinct mutations at Y132 in the donor's FL (Y132N, VAF 17%) and the recipient's FL (Y132S, VAF 8%), respectively.



(legend on next page)

cells, another human B-cell lymphoma cell line (Figures S1B and S1C). Overexpression of CTSS WT (CTSS^{WT}) or CTSS Y132D (CTSS^{Y132D}) in DG75 CTSS^{KO} cells similarly showed an increased ratio of mature CTSS to the inactive proform of CTSS (pro-CTSS) in the presence of the Y132D mutation (Figure 2B).

We next aimed to quantify the *in vitro* proteolytic activity of CTSS. Therefore, we purified CTSS from Karpas422 cells with or without the Y132D mutation by immunoprecipitation using a polyclonal anti-CTSS antibody. Immunoprecipitates showed comparable protein levels of mature CTSS and pro-CTSS (Figure 2C, left) as well as similar ratios of mature CTSS to pro-CTSS (Figure 2C, right). We used these immunoprecipitates to cleave Z-VVR, a synthetic CTSS substrate labeled with the fluorochrome amino-4-trifluoromethyl coumarin (AFC). Immunoprecipitates from CTSS Y132D mutant clones showed significantly increased substrate cleavage activity over time, to approximately 3-fold after 16 h compared to CTSS^{WT} (Figures 2D and S2B–S2D). The addition of the CTSS inhibitor *trans*-Epoxysuccinyl-L-leucylamido(4-guanidino)butane (E-64) resulted in a complete loss of proteolytic activity of both CTSS^{Y132D} and CTSS^{WT}. Another Y132 mutation, Y132S, showed a similarly increased CTSS substrate cleavage activity over time (Figure S2D). As an additional control, we generated a catalytic dead mutant of CTSS (C139A) (Kaulmann et al., 2006). As expected, CTSS with both Y132D and C139A mutations showed a complete loss of function (Figure S2E).

Notably, we previously hypothesized that another CTSS mutation, M185V, is likely a passenger rather than a driver mutation of lymphomagenesis (Weigert et al., 2012). Specifically, in the case of donor-derived FLs described before, a CTSS M185V mutation was detectable in the donor's FL and the donor-derived common precursor clone but only in a small subclone of the FL that developed in the BMT recipient. Thus, we also tested the *in vitro* cleavage activity of this CTSS mutation. As expected, CTSS M185V did not increase substrate cleavage activity compared to CTSS^{WT} (Figure S2F).

Y132D Accelerates Autocatalytic CTSS Activation

Based on the above data, we hypothesized that CTSS Y132 mutations induce accelerated conversion from pro-CTSS to mature CTSS. To quantify mutation-specific differences in CTSS conversion kinetics, we developed a strategy to purify only full-length pro-CTSS. A single FLAG-tag sequence was introduced between the SP and pro-CTSS (Figure 3A) to maintain correct subcellular compartment targeting and proper protein folding.

FLAG-tagged pro-CTSS^{WT} and FLAG-tagged pro-CTSS^{Y132D} were then cloned into a tetracycline-controlled expression vector and transiently expressed in 293T cells. Doxycycline treatment induced similar levels of FLAG-pro-CTSS^{WT} and FLAG-pro-CTSS^{Y132D} (Figure 3B). Pull-down with anti-FLAG yielded highly purified pro-CTSS^{WT} and Y132D proteins (Figure 3C, left side). These were used to again demonstrate the increased substrate cleavage activity of Y132D over time. Notably, the steeper slope of Y132D leveled out after 2 to 4 h, indicating that—once converted—active CTSS^{Y132D} and CTSS^{WT} have similar proteolytic activities (Figure 3C, right side). Indeed, when we started with similar amounts of highly purified pro-CTSS and allowed complete *in vitro* conversion to active CTSS before testing substrate cleavage activity, we no longer observed differences between WT and Y132D (Figure S3A).

We then assayed the *in vitro* autocatalytic cleavage of pro-CTSS^{WT} and pro-CTSS^{Y132D} over time at catalytic (i.e., endolysosomal like) conditions as previously described (Vasiljeva et al., 2005). SDS-PAGE and silver staining confirmed accelerated autocatalytic conversion from pro-CTSS to mature CTSS (Figure 3D). To quantify the relative differences in conversion kinetics, we performed densitometry in 3 independent replicates. The time required to convert 50% of pro-CTSS decreased from 17 min for WT to 11 min for Y132D (Figure 3E).

We conclude that Y132D does not increase the activity of the mature enzyme but is a gain-of-function mutation by accelerating the conversion from pro-CTSS to catalytically active mature CTSS.

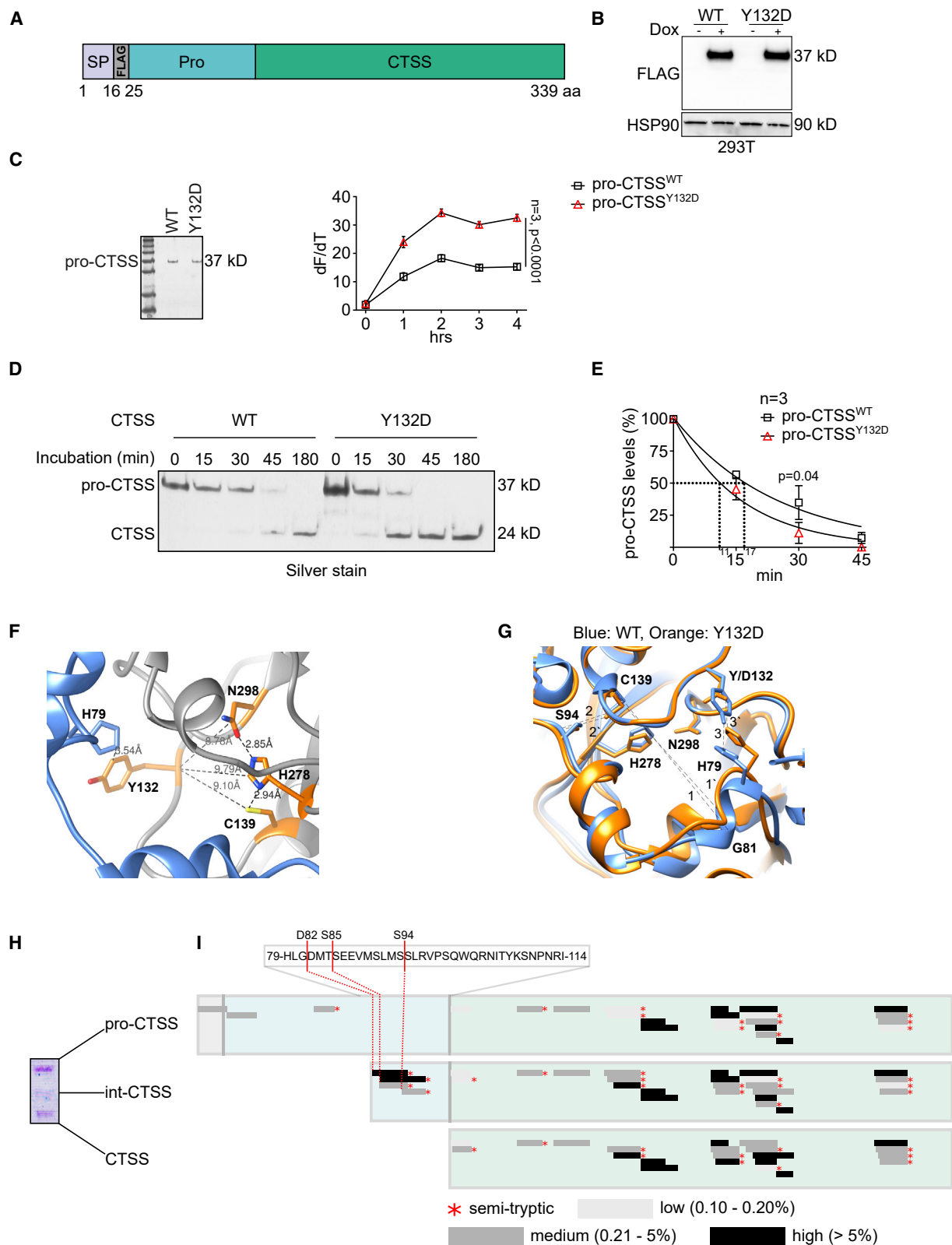
Molecular Simulations and Mass Spectrometry Reveal Y132D-Induced Structural Changes

The 3-dimensional structure of pro-CTSS (McGrath et al., 1998) revealed that Y132 does not directly interact with the catalytic triad (C139, H278, and N298), confirming our observation that mutations at this position do not directly alter the proteolytic activity of the mature enzyme (Figure 3F). However, the Y132 residue forms a hydrogen bond with H79 of the propeptide (Figure 3F). Thus, we hypothesized that substituting Y132 (WT) by D132 (mutant) might bring the catalytic triad closer to the propeptide, thereby facilitating autocatalytic cleavage.

To model the structural effect of the Y132D mutation, we performed molecular dynamics (MD) simulations under acidic conditions. Starting from the published CTSS structure, we calculated the distances between molecules after the introduction of the mutation over a fixed period of time. A previously

Figure 2. CTSS Y132 Mutations Are Gain-of-Function and Increase Substrate Cleavage Activity

(A) Western blot of Karpas422 cells with CTSS wild-type (WT) or CRISPR-Cas9-engineered single-cell-derived clones with CTSS^{Y132D} (#E2 and #H41) or CTSS knockout (KO) with normalized ratio of mature (cleaved) CTSS/pro-CTSS protein levels from 3 different western blots. See also Figures S1 and S2A.
(B) Similar to (A) with CTSS^{WT} or CTSS^{Y132D} re-expressed in DG75 CTSS^{KO} cells.
(C) Western blot of CTSS immunoprecipitates (IP) from cells from (A) with normalized ratios of mature CTSS/pro-CTSS, from 3 different western blots. DG75 CTSS^{KO} cells were used as negative control. Asterisks indicate immunoglobulin G (IgG) light chains slightly above CTSS.
(D) CTSS substrate cleavage over 24 h. Z-VVR-AFC was used as a CTSS substrate; E-64 was used as a cathepsin inhibitor. Similar results were obtained with the cathepsin inhibitor Z-FF-fluoromethyl ketone (FMK). $\Delta F(\text{CTSS})/\Delta F(\text{S})$ is the fold change compared to the AFC signal without the enzyme added. Goat IgG antibody without antigen specificity was used as a negative control for the IP (control). See Figures S2C–S2F for substrate cleavage activity of CTSS Y132S, M185V, and C139A and from Karpas422 CTSS^{KO} cells. Each time point from 6 independent IPs was measured twice.
Band intensities of gels were quantified using ImageJ densitometry (also in all subsequent figures). Pooled data from biological replicates (n) are represented as mean \pm SD in Figures 2A–2D; p values are from unpaired Student's t test.



(legend on next page)

described, an autocatalytic cleavage site between S93-S94 results in an intermediately sized protein (Quraishi and Storer, 2001). At early time points of MD simulations (10.1–25 ns), C139 is indeed closer to S94 for D132 than Y132 (Figure S3B). However, with an increasing simulation time, the C139-S94 distance increases again and is essentially similar for Y132 and D132 at later time points (105–110.1 ns). In contrast, the molecular distances between C139 and L80, G81, and D82 decrease for D132, whereas these distances remain essentially unchanged for Y132 (Figures 3G and S3C–S3E). The shorter distances between C139 of the catalytic triad and a stretch of peptides from the proform (between H79 and I114) might facilitate intramolecular cleavage and potentially yield several intermediate-sized proteins.

To experimentally validate our model, we gel-purified different-sized CTSS proteins (Figure 3H) and performed liquid chromatography-tandem mass spectrometry (LC-MS/MS). In addition to pro-CTSS and mature CTSS, we indeed identified an intermediate-sized CTSS band (Figure 3H). Interestingly, we could detect semi-tryptic peptide sequences supporting two autocatalytic cleavage sites: G81-D82 and T84-S85. Both are in close proximity to the reported cleavage site S93-S94, which was also detected in the LC-MS/MS data, although with a lower peptide intensity (Figure 3I). Overall, our structural and experimental data support the following molecular mechanism: Y132 mutations result in intramolecular structural changes with shortening of the distances between the catalytic site of CTSS and several cleavage sites within the propeptide, which facilitates and accelerates autocatalytic conversion from pro-CTSS to several intermediate-sized forms and, subsequently, to the mature CTSS protein.

CTSS^{Y132D} Increases Antigen-Specific CD4⁺ T Cell Responses

CD74 is a well-recognized physiologic CTSS substrate and plays critical roles in the assembly, trafficking, and stabilization of peptide-free MHC class II heterodimers (Anderson and Miller, 1992). In endolysosomes, CD74 undergoes sequential degradation by various proteases, including CTSS, leaving the small CLIP fragment occupying the antigen-binding groove of MHC class II (Riese et al., 1996). CTSS ultimately cleaves and releases CLIP,

thereby allowing binding and presentation of antigens on MHC class II to antigen-specific CD4⁺ T cells (Rückrich et al., 2006). Thus, we hypothesized that CTSS^{Y132D} may enhance CD74/CLIP cleavage and augment CD4⁺ T cell activation.

Indeed, we observed decreased full-length CD74 (p34) protein levels and more cleaved CD74 fragments in Karpas422 clones with CTSS^{Y132D} mutations (#E2 and #H41) than in CTSS^{WT} cells. Treatment with the cathepsin inhibitor E-64 nearly completely abolished CD74 cleavage (Figure 4A, left). Similar results were observed for DG75 CTSS^{KO} cells overexpressing either CTSS^{WT} or CTSS^{Y132D} compared to the empty vector (EV) control (Figure 4A, right).

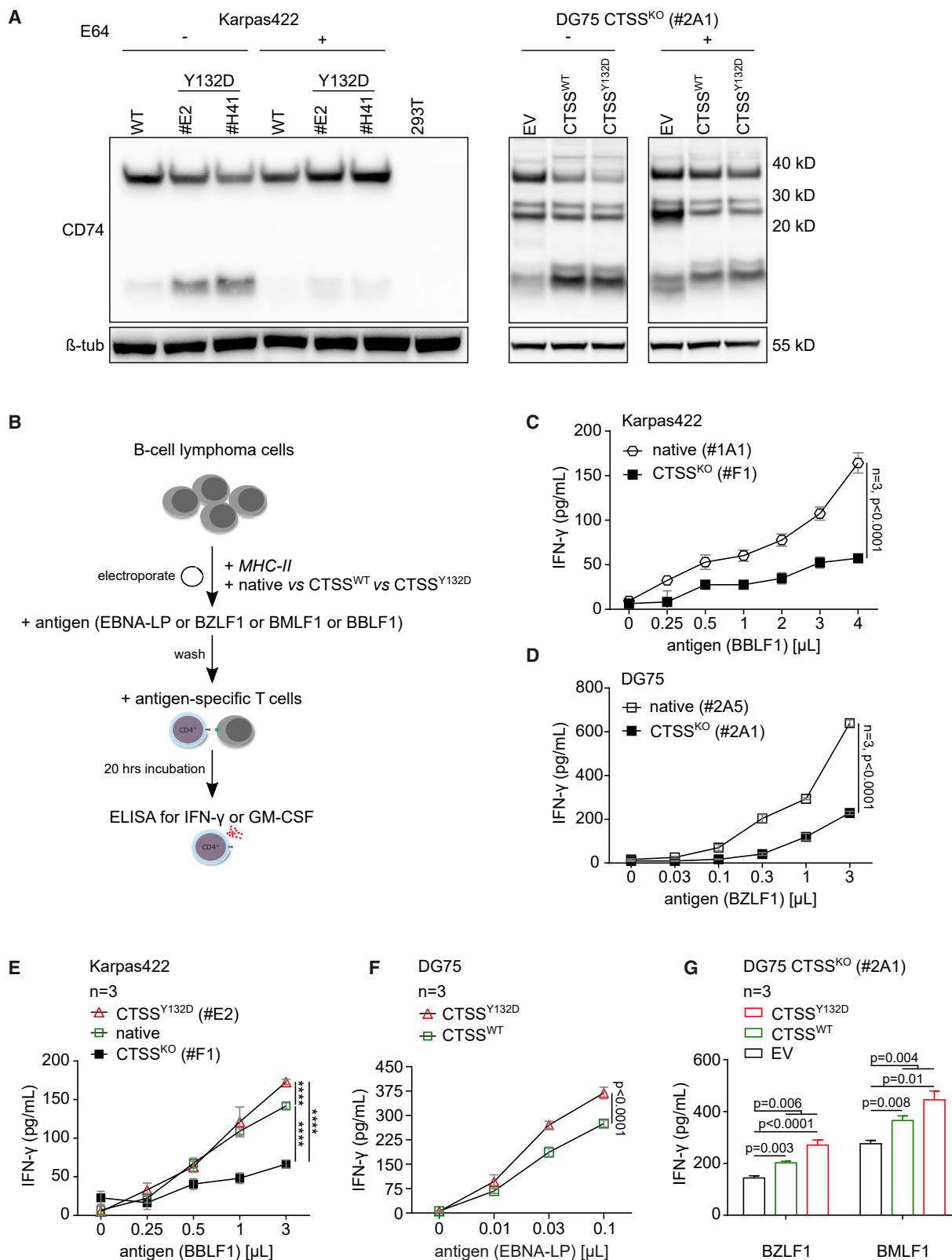
To study the impact of CTSS^{Y132D} on antigen-specific CD4⁺ T cell activation, we used an established co-culture assay (Fiebigger et al., 2012). Briefly, human B-cell lymphoma cells (DG75), which do not have a CTSS mutation, were transfected to overexpress CTSS^{WT} or CTSS^{Y132D} along with MHC class II. The cells were then incubated with increasing amounts of EBV (Epstein-Barr virus) recombinant antigens (BBLF1, BZLF1, BMLF1, or EBNA-LP). Next, cells were washed and antigen-specific CD4⁺ T cells derived from healthy EBV-infected donor(s) were added. After co-culturing for 20 h, T cell activation was quantified by measuring cytokine release (Figure 4B). In similar experiments, we used Karpas422 cells, comparing native (CTSS^{WT}) versus CTSS^{KO} versus CTSS^{Y132D} clones for their ability to induce antigen-specific T cell responses. Importantly, CTSS^{Y132D} is highly unlikely to be immunogenic per se, as bioinformatics analyses demonstrated that CTSS Y132 is not predicted to bind to any representative MHC class II (25 histocompatibility leukocyte antigen [HLA]-DR, 20 HLA-DQ, and 9 HLA-DP) alleles (Figure S4A).

First, we demonstrated that Karpas422 CTSS^{KO} and DG75 CTSS^{KO} cells have severely impaired CD4⁺ T cell activation capacity upon antigen stimulation, as measured by low interferon γ (IFN- γ) levels, compared to native cells (Figures 4C and 4D). This confirms that CTSS activity is a major determinant of antigen-specific CD4⁺ T cell activation in our co-culture experiments.

Next, we compared CTSS^{WT} (native) and CTSS^{Y132D} in Karpas422 cells. Although CTSS is expressed at similar (endogenous) levels in these cells (Figure S2A), the higher activity of

Figure 3. Y132D Accelerates Autocatalytic CTSS Activation

- Schematic of full-length CTSS with FLAG inserted between the SP and the pro-enzyme.
- Western blot of HEK293T cells (293T) with Tet-inducible FLAG-tagged pro-CTSS (WT or Y132D).
- CTSS substrate cleavage assay from 3 independently purified proteins over 4 h by using purified pro-CTSS (Y132D versus WT), visualized in a silver-stained SDS-PAGE; dF/dt, rate of the reaction. See Figure S3A for CTSS substrate cleavage activity of completely converted mature CTSS (WT and Y132D).
- In vitro* autocatalytic processing of purified pro-CTSS to mature CTSS (WT and Y132D) over time at endolysosomal-like conditions (pH 5.5); silver-stained SDS-PAGE.
- Non-linear fitting analysis of band intensities from 3 independent protein conversions from (D). CTSS half-life indicated by dotted lines.
- Published crystal structure of human pro-CTSS (PDB: 2C0Y). The conformation of the catalytic triad (C139, H278, and N298) and distances to Y132 are shown. The distance between selected atoms of H79 and Y132 is also shown. The pro-sequence is depicted in blue.
- Snapshot of the MD simulation at 108.3 ns. Blue, pro-CTSS^{WT}; orange, pro-CTSS^{Y132D}. Distances (dashed lines) between molecules: 1 = 19.16 Å (WT: C139-G81); 1' = 17.66 Å (Y132D: C139-G81); 2 = 5.84 Å (WT: C139-S94); 2' = 5.84 Å (Y132D: C139-S94); 3 = 3.27 Å (WT: Y132-H79); 3' = 2.87 Å (D132-H79). See Figures S3B–S3E for MD simulation time courses.
- Coomassie-blue-stained SDS-PAGE with protein bands used for mass spectrometry.
- LC-MS/MS analysis of pro-, intermediate (int)-, and mature CTSS. Red lines mark plausible autocatalytic cleavage sites (D82, S85, and S94) within the propeptide. Asterisks indicate semitryptic peptides. Peptide frequencies are represented with different gray tones. Pooled data from biological replicates (n) are represented as mean \pm SD; p values are from unpaired Student's t test.



(legend on next page)

CTSS^{Y132D} led to increased antigen-specific T cell activation with increasing doses of antigen (BBLF1) (Figure 4E). Similarly, DG75 overexpressing CTSS^{Y132D} activated CD4⁺ T cells more efficiently than overexpression of CTSS^{WT} with increasing doses of the EBNA-LP antigen (Figure 4F). In fact, we could consistently show the higher capacity of DG75 CTSS^{Y132D} over CTSS^{WT} over EV control to stimulate antigen-specific CD4⁺ T cells responses, using different antigens (Figures 4G, S4B, and S4C), using T cells from different donors (Figure S4B), and measuring different cytokines (IFN- γ and granulocyte-macrophage colony-stimulating factor (GM-CSF) in Figure S4C) released by activated T cells.

Moreover, CTSS is known to process antigens within the vacuolar pathway of cross-presentation, ultimately leading to CD8⁺ T cell activation (Shen et al., 2004). However, we did not observe differences between CTSS^{Y132D}, CTSS^{WT}, and EV control in activating antigen-specific CD8⁺ T cells (Figures S4D and S4E).

Hence, our data demonstrate that increased CTSS activity in lymphoma cells, either by CTSS^{Y132D} mutation or overexpression of CTSS^{WT}, leads to enhanced activation of antigen-specific CD4⁺ but not CD8⁺ T cells.

Hyperactive CTSS Promotes Tumor Growth *In Vivo*

Based on our data, we hypothesized that aberrant CTSS hyperactivity in FL is a later acquired (often subclonal) event, leading to CD4⁺ T cell activation and tumor progression. In fact, previous work has shown that CD4⁺ T cells can support the growth of human FL cells *in vitro* (Scott and Gascoyne, 2014; Umetsu et al., 1990) and in an *in vivo* mouse model (Scott and Gascoyne, 2014; Tsiagbe et al., 1993).

To functionally link aberrant CTSS hyperactivity with lymphoma growth, we used the following experimental model: we generated A20 B-cell lymphoma cells (derived from BALB/c mice) (Kim et al., 1979) expressing EV, CTSS^{WT} (CTSS^{hi}), or CTSS^{Y132D} (all GFP-labeled) (Figure S5A). First, we confirmed increased CTSS expression in A20 CTSS^{hi} and an increased ratio of mature CTSS to pro-CTSS in A20 CTSS^{Y132D} by western blot and densitometry (Figure 5A). Next, we confirmed significantly increased *in vitro* substrate cleavage activity of immunoprecipitated CTSS^{Y132D} from these cells, which could be completely inhibited by the cathepsin inhibitor E-64 (Figure 5B). We monitored *in vitro* growth kinetics of these cells and did not detect any differences in 3 independent experiments (Figure 5C).

We then vaccinated BALB/c mice with sheep red blood cells (SRBCs) and mixed splenocytes from these mice with the transduced A20 lymphoma cells (Figure S5B). This model captures germinal center (GC)-like immune cell infiltration and facilitates the interaction between A20 lymphoma cells and syngeneic immune cells. The mixtures were injected into immunocompetent BALB/c recipients and then tumor progression was tracked (Figure 5D). Unlike results *in vitro*, CTSS hyperactivity in A20 cells (CTSS^{Y132D} and CTSS^{hi}) resulted in accelerated tumor growth *in vivo* compared to EV controls in 2 separate experiments (Figures 5E and S5C).

CTSS Hyperactive Mouse Tumors Show Increased CD4⁺ T Cell Infiltration and Immune Activation

We sacrificed mice and collected the tumors from the second experiment for further analyses at day 19, when tumors in the CTSS^{Y132D} and CTSS^{hi} cohorts started to outgrow EV controls (Figure S5C). Representative immunohistochemistry (IHC) stains are shown in Figure 5F. CTSS^{Y132D} and CTSS^{hi} tumors showed significantly higher CD4⁺ T cell infiltration than EV controls (Figures 5F and 5G), whereas CD8⁺ T cell infiltrations were generally low (Figure 5F). Furthermore, CTSS^{Y132D} tumors showed higher CD4⁺/CD8⁺ T cell ratios by IHC (Figure 5H) and flow cytometry (Figure S5D), as well as significantly increased IFN- γ levels (Figure 5I).

Overall, the data of this FL model shows that hyperactive CTSS (CTSS^{hi} or CTSS^{Y132D}) promotes tumor growth *in vivo* by inducing an activated immune microenvironment characterized by increased CD4⁺ T cell infiltration and proinflammatory cytokine perturbation.

Human FL Biopsy Samples with CTSS Y132 Mutations Have Gene Expression Profiles Linked with Antigen Processing and Chemokine Perturbation

To identify differences in immune response pathways of the tumor microenvironment in human FL, we applied a 730-immune gene expression panel (PanCancer Immune Profiling; NanoString) to primary tumor biopsy samples from patients with previously untreated FL with (N = 9) or without (N = 43) CTSS Y132 mutations. This approach is certainly biased toward detecting changes in immune-related genes. Nevertheless, comparison of these immune profiles showed interesting patterns of

Figure 4. CTSS^{Y132D} and CTSS^{WT} Overexpression Increase Antigen-Specific CD4⁺ T Cell Responses *In Vitro*

(A) Western blot for CD74 in Karpas422 with CTSS^{WT} or Y132D (#E2 and #H41) and DG75 CTSS^{KO} cells expressing empty vector (EV), CTSS^{WT}, or CTSS^{Y132D}. E-64 was used as a cathepsin inhibitor. HEK293T cells were used as a negative control. The experiment is representative of 3 independent replicates for both cell lines.

(B) Schematic overview of the *in vitro* co-culture experiment.

(C) Karpas422 native (#1A1, CTSS^{WT}) and CTSS^{KO} (#F1) single-cell-derived clones were incubated in 3 different wells with increasing antigen doses (BBLF1) and co-cultured with BBLF1-specific CD4⁺ T cells (clone HDe). IFN- γ in the supernatant was measured by ELISA (also in subsequent subfigures).

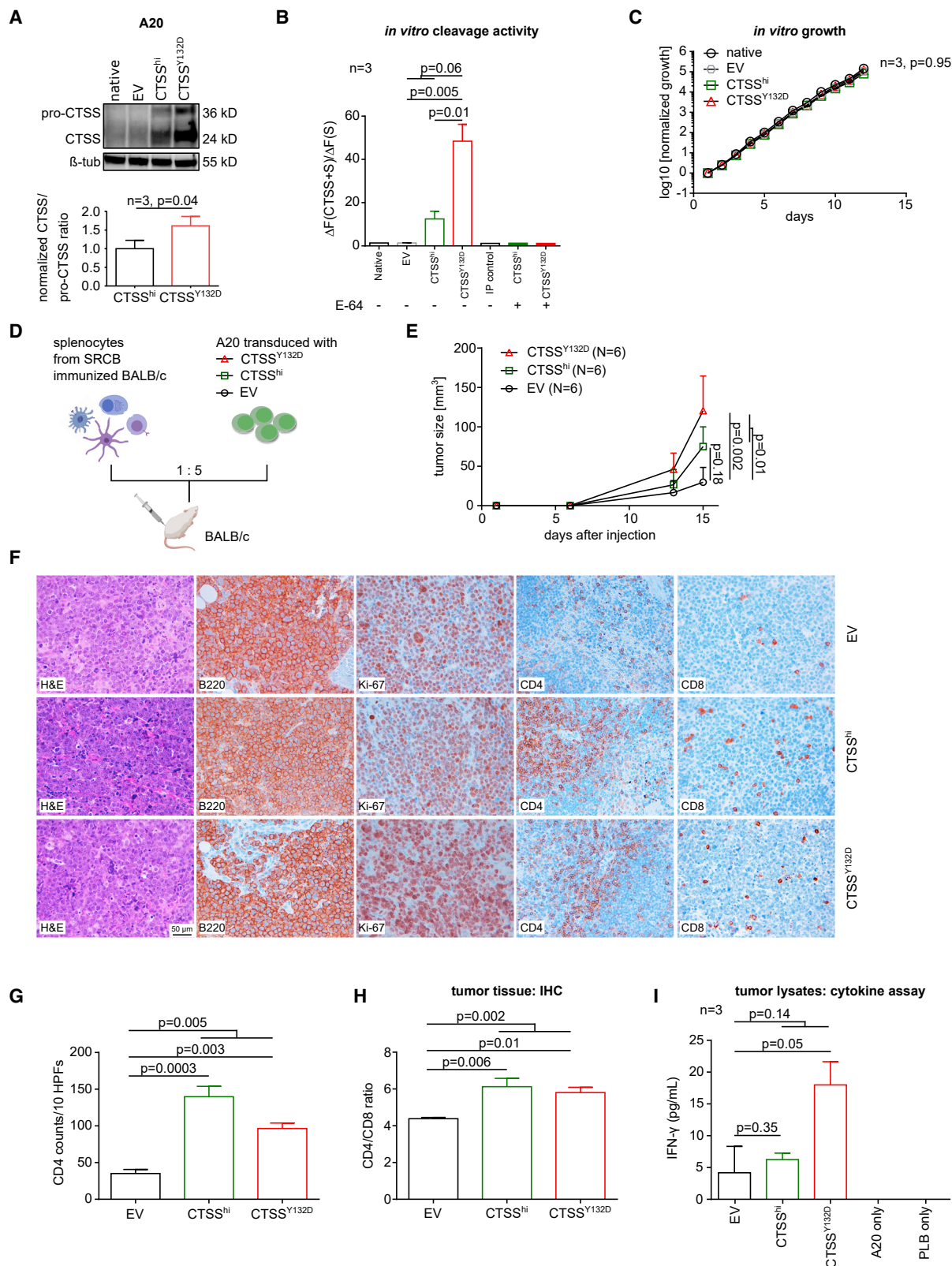
(D) Similar to (C), DG75 native (#2A5, CTSS^{WT}) and DG75 CTSS^{KO} (#2A1) single-cell-derived clones were incubated with increasing antigen doses (BZLF1) and co-cultured with BZLF1-specific CD4⁺ T cells (clone 3H11).

(E) Similar to (C), using Karpas422 CTSS^{Y132D} single-cell-derived clones (#E2) in the assay.

(F) DG75 native cells were transfected with CTSS expression constructs (WT or Y132D) along with the restricting MHC class II allele. Cells were incubated with increasing antigen concentrations (EBNA-LP) and co-cultured with antigen-specific CD4⁺ T cells (clone 3#1).

(G) DG75 #2A1 CTSS^{KO} cells were transfected with EV, CTSS^{WT}, or CTSS^{Y132D} together with expression plasmids coding for BZLF1 or BMLF1. Twenty h later, the cells were probed with BZLF1- and BMLF1-specific CD4⁺ T cells. See Figure S4 for replicate experiments with different T cell clones, antigens, and cytokine readout. All ELISA measurements were performed in technical triplicates (also in subsequent figures).

Pooled data from biological replicates (n) are represented as mean \pm SD; p values are from unpaired Student's t test; ****p < 0.0003.



(legend on next page)

differentially expressed genes, most notably for chemokines, including CXCL13, a B-cell chemoattractant that is produced by CD4⁺ T_{FH} cells, as well as genes involved in antigen processing and presentation, such as the MHC class II genes HLA-DQA1 and HLA-DQB1 (Figure 6A). Reminiscent of our mouse data, IFN- γ was among the upregulated genes, as well as its receptor (INF- γ R1). Gene set analysis revealed that the top differentially expressed genes were enriched within the biological pathways antigen processing and chemokines (Figure 6B). These data support the hypothesis that CTSS hotspot mutations are, indeed, linked with increased antigen processing and proinflammatory chemokine response in human FL.

Integrated Analysis of CTSS Mutations, Amplifications, and Gene Expression in Human FL

CTSS is located at 1q21, and this locus is known to be frequently amplified in FL (Rao et al., 1998). Chromosome genomic array testing (CGAT; OncoScan) was available for 146 primary tumor biopsy samples from patients with advanced FL. Furthermore, we inferred CTSS amplification status from another 140 FL by using DNA sequencing data and a bioinformatics pipeline (CNVkit) capable of identifying amplification status that correlated well with CGAT data ($R = 0.91$, $p = 2.2 \times 10^{-16}$) (Figure S6A). Overall, data from 286 FL were available for analysis of CTSS mutation and amplification status. A total of 49 cases (17%) had CTSS Y132 mutations or CTSS amplifications. Notably, CTSS Y132 mutations and CTSS amplifications were mutually exclusive (Figure 6C). Therefore, we hypothesized that CTSS amplification might be linked to increased gene expression and constitute an alternative mechanism of increasing CTSS activity in FL. We analyzed a total of 51 diagnostic FL biopsy samples with available CTSS CN status and CTSS gene expression data. Generally, FLs with CTSS CN gain had, indeed, higher CTSS expression (Figure S6B). Using *k*-means clustering, we identified 11 cases with high CTSS expression (22%), including 8 cases with CTSS CN neutral, which suggests additional mechanisms of transcriptional dysregulation of CTSS. To further support our hypothesis that the malignant B cells are the source of aberrantly increased CTSS expression in a subset of FL, we analyzed publicly available transcriptome data obtained from B cells from 5 normal GCs (centroblasts [CBs] and centrocytes [CCs]), 4 normal blood samples (peripheral blood B cells

[pBBCs]), and 16 FL biopsy samples (Koues et al., 2015). By *k*-means clustering, we indeed identified a subset of FLs (11/16), which had significantly higher CTSS expression levels than normal CBs and CCs (Figure 6D), the normal counterpart (i.e., cells of origin) of FL.

Overall, our integrated analyses reveal that CTSS can be aberrantly hyperactivated in FL cells by several alterations, including (1) accelerated conversion to active CTSS by CTSS Y132 mutations and (2) CTSS overexpression by either CN gain or transcriptional dysregulation.

CTSS Hyperactivity Is Associated with an Activated, CD4⁺ T Cell Enriched Immune Microenvironment in Human FL

Next, we asked whether CTSS hyperactivity is also linked with an activated immune microenvironment in human FL, as has been observed in our preclinical mouse model. Therefore, we first quantified CD4⁺ T cells in 15 primary FL biopsy samples by IHC. Representative IHC stains are shown in Figure 6E. FL with high CTSS expression (CTSS^{hi}) and FL with CTSS^{Y132D} mutations had higher intrafollicular CD4⁺ T cell infiltration than FL without CTSS Y132 mutations and low CTSS expression (CTSS^{WT+low}). Next, we showed that intrafollicular CD4⁺ T cell abundance correlates with *CD4* gene expression (Figure 6F). This allowed us to systematically analyze all FL with available gene expression data. Expressions of CTSS and *CD4* were significantly correlated (Figure 6G). Notably, FL with hyperactivated CTSS (CTSS^{hi} and/or CTSS^{Y132D}) generally showed higher ratios of *CD4/CD8* (Figures S6C–S6E) and was most pronounced for CTSS^{Y132D} FLs (Figure 6H). This closely mirrors our preclinical data (Figures 5H and S5D). Lastly, as PDL2 has been proposed to serve as a surrogate marker of increased immune cell infiltration (Tobin et al., 2019), we tested its interaction with CTSS expression levels and confirmed a highly significant positive correlation (Figure 6I).

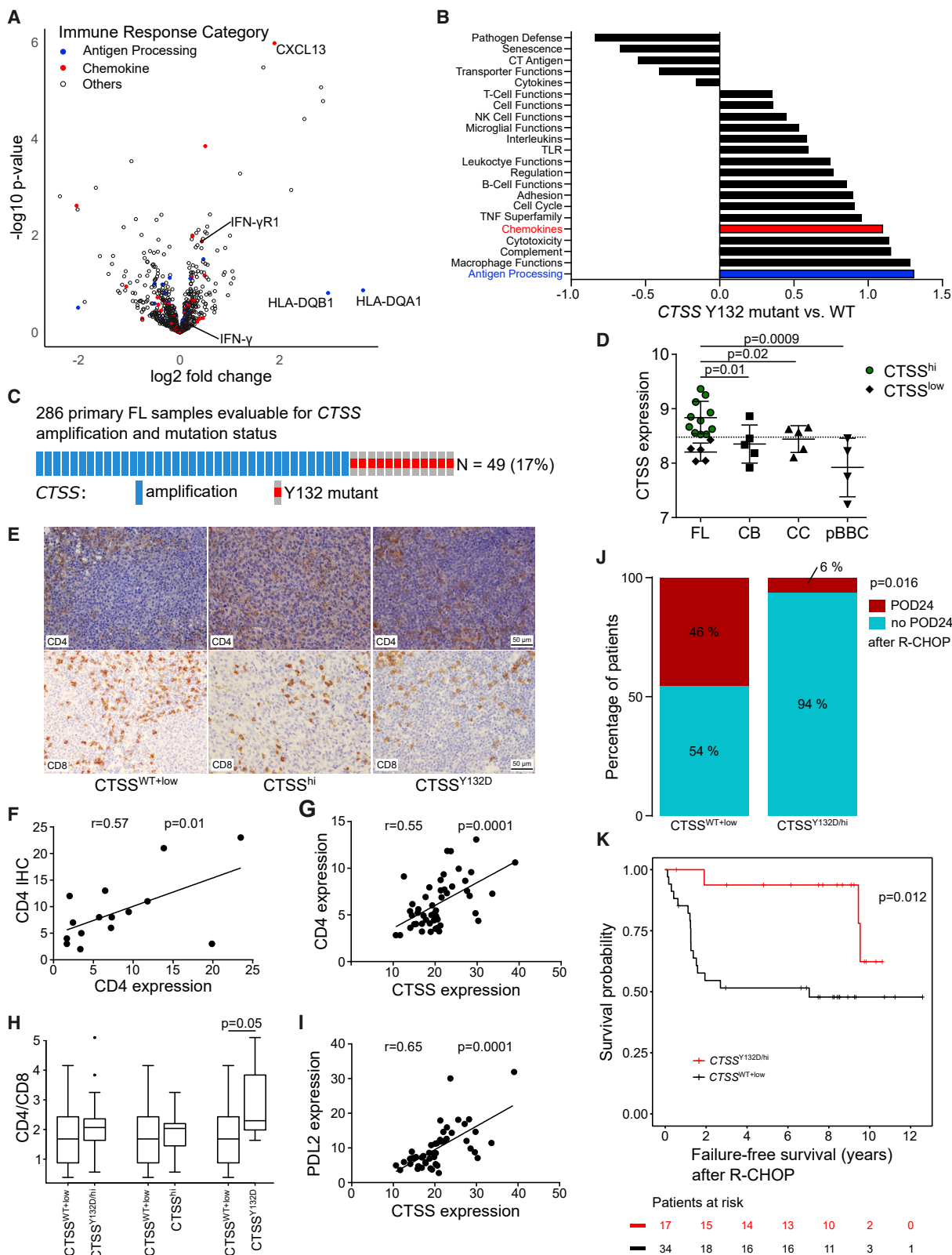
CTSS Hyperactivity Is Associated with Better Treatment Outcome in Patients Receiving Immunochemotherapy

Our data show that aberrant CTSS hyperactivity in FL can induce and activate a CD4⁺ T cell enriched immune microenvironment and is correlated with high PDL2 expression. We have previously shown that high PDL2 expression is a promising biomarker to

Figure 5. Hyperactive CTSS Accelerates Tumor Growth in Immunocompetent Mice

- (A) Western blot with quantification using 3 different lysates from stably transduced A20 cells; mean intensity \pm SD.
- (B) CTSS substrate cleavage activity after 16 h. Z-VVR-AFC was used as a CTSS substrate; E-64 was used as a cathepsin inhibitor. The substrate cleavage activity after 16 h from 3 independent IPs was measured twice; mean activity \pm SD.
- (C) Normalized log₁₀ *in vitro* growth using 3 independent flasks of stably transduced A20 cells; mean cell growth \pm SD.
- (D) Experimental overview. Splenocytes (0.2×10^6) from sheep red blood cell (SRBC)-immunized BALB/c mice were mixed 1-to-5 with stably transduced A20 cells (1×10^6). A total of 1.2×10^6 cells were then injected per BALB/c mouse. $N = 6$ mice per group (WT versus Y132D versus EV).
- (E) Tumor growth and tumor volume were measured at indicated time points after injections from (D). See Figure S5C for repeat experiment with 1×10^5 A20 cells mixed with 0.2×10^5 splenocytes and Figures S5A and S5B for FACS analyses of the pre-injection cell mix; *p* values are indicated for day 16; tumor size is depicted as mean \pm SEM.
- (F) Immunohistochemistry (IHC) of formalin-fixed isolated mouse tumors for H&E, B220, Ki-67, CD4, and CD8; scale bar is 50 μ m.
- (G) CD4 counts per 10 high-power fields (HPFs) from (F) using 2 (EV) or 3 (CTSS^{hi} and CTSS^{Y132D}) different mouse tumors; mean counts \pm SD.
- (H) CD4 versus CD8 ratio based on counts per 10 HPFs from IHC. See also Figure S5D for FACS analysis of isolated tumor suspensions; mean counts \pm SD.
- (I) IFN- γ measurement in tumors lysed with passive lysis buffer (PLB) ($n = 3$). A20 cells and PLB only were used as negative controls. E-64 was used as a cathepsin inhibitor; mean signal \pm SD.

All *p* values result from unpaired Student's *t* test.



(legend on next page)

identify patients who are at risk for early treatment failure, i.e., progression of disease within 24 months (POD24) (Tobin et al., 2019). This prompted us to explore whether aberrant CTSS hyperactivity is associated with treatment outcome in FL. We only analyzed patients who uniformly received standard immunochemotherapy (Rituximab [R]-cyclophosphamide, doxorubicin, vincristine, prednisone [CHOP] or R-CHOP) for previously untreated, symptomatic, advanced FL (Pastore et al., 2015) with known CTSS mutation and CTSS gene expression status from their pretreatment biopsies (Figure 6K). FL with CTSS Y132 mutations (N = 6) or CTSS overexpression (by top *k*-means cluster, N = 11) were grouped into one cohort (CTSS^{Y132D/hi}, N = 17) and compared to FL without CTSS Y132 mutations and low CTSS expression (CTSS^{WT+low}, N = 34). In fact, only 6% of patients with CTSS^{Y132D/hi} FL experienced POD24, compared to 46% of patients with CTSS^{WT+low} FL (Figure 6J; *p* = 0.016). This translated into longer failure-free survival (FFS) (Figure 6K) and overall survival (OS) after R-CHOP (Figure S6F) in patients with CTSS-hyperactive FL.

Validation Studies in an Independent Patient Cohort

Finally, we aimed to validate our findings in an independent patient cohort. We reanalyzed sequencing data from 174 patients with FL from a prospectively maintained clinical lymphoma database that was reported previously (Tobin et al., 2019). CTSS mutations were identified in 6 cases (3.4%), with all but one consisting of Y132D (Figure 7A). RNA was available from 104 cases and analyzed by digital multiplexed gene expression profiling. We excluded 30 cases from further analyses, as these patients did not require or receive systemic treatment within 1 year of diagnosis. Notably, none of these 30 patients with asymptomatic, low burden disease had detectable CTSS mutations. Using *k*-means clustering, we classified 37 cases as CTSS^{hi} (50%). Again, CTSS expression levels correlated significantly with CD4 (*p* = 0.0026) and PDL2 expression (*p* < 0.0001) (Figures S7A and S7B).

Pretreatment biopsy samples from 12 patients were available for digital multispectral imaging (Vectra Polaris) of immune cell markers (CD4, CD8, PD1, PDL1, and PDL2), allowing automated quantification and spatial resolution of immune cell infiltrates.

Representative pictures are shown in Figure 7B. A tonsil from a healthy donor served as a staining control (Figure S7C). Overall, CTSS^{hi} FL and CTSS^{Y132D} FL showed higher CD4⁺ T cell infiltration than CTSS^{WT+low} FL (Figure 7C). CD4⁺ T cell abundance and spatial distribution appeared to inversely correlate with CD8⁺ T cells (Figures 7B and 7C) and to positively correlate with markers of an activated immune microenvironment, including PDL2 (Figures 7B and S7B). Intrafollicular CD4⁺ T cell infiltrates showed diffuse patterns in CTSS^{hi} FL and patchy distribution in CTSS^{Y132D} FL (Figure 7B), confirming previous observations from IHC (Figure 6E). At a higher magnification, CD4⁺ T cells in CTSS^{Y132D} FL were frequently observed in close proximity to highly proliferating FL cells (Figure 7B, bottom panel), further supporting our hypothesis that CTSS Y132 mutations—even if present only in FL subclones—are tumor-promoting alterations.

For the analysis of treatment outcome, we again only analyzed patients who received standard immunochemotherapy (R-CHOP, or R-cyclophosphamide, vincristine, prednisone [R-CVP], or R-bendamustine, N = 72). We validated our previous finding that patients with CTSS^{Y132D/hi} FL had lower rates of POD24 than patients with CTSS^{WT+low} FL (9% versus 29%, *p* = 0.057) (Figure 7D). We also observed a trend toward longer FFS in patients with CTSS-hyperactive FL (Figure 7E).

DISCUSSION

Here, we provide evidence of positive selection for aberrantly increased CTSS activity in FL. Although detectable in less than 10% of cases, somatic missense mutations in CTSS cluster at a single mutational hotspot, Y132. Independent acquisition of distinct CTSS Y132 mutations in a case of donor-derived FLs impressively illustrates convergent evolution. Functional data and structural modeling show that Y132D mutations are gain-of-function by accelerating conversion from enzymatically inactive pro-CTSS to a proteolytically active CTSS. Although Y132S similarly increases *in vitro* cleavage activity, Y132D (TAT > GAT) is by far the most frequent CTSS mutation. The reason for this preference could be related to the biological process of generating this mutation. Alexandrov et al. (2013) have described a distinct mutational signature (signature 9) in malignant B-cell

Figure 6. CTSS Hyperactivity Is Associated with an Activated Immune Microenvironment in Pretreatment Human FL Biopsies and Has Clinical Impact on Patients Receiving Standard Immunochemotherapy

- (A) Immune gene expression profiling of primary patient samples (PanCancer Immune Profiling; nCounter, NanoString). Volcano plot showing differentially expressed genes for CTSS Y132 mutant FL (N = 9) versus CTSS^{WT} FL (N = 43).
- (B) Direct global significance score analysis from (A) for each annotated gene set.
- (C) OncoPrint for primary FL samples with CTSS copy number (CN) gain (blue) and CTSS Y132 mutations (red) within our cohort of evaluable FL (N = 286).
- (D) Normalized CTSS expression from transcriptome data from sorted malignant and non-malignant B-cells (CB, centroblasts; CC, centrocytes; pBBCs, peripheral blood B-cells). FL samples with high CTSS expression were identified by *k*-means clustering (green dots above dashed line); *p* values are from unpaired Student's *t* test.
- (E) Representative IHC stains for CD4 and CD8 in pretreatment FL biopsies. See Figure S6C for CD4/CD8 ratios based on IHC counts; scale bars are 50 μ m.
- (F) Number of CD4⁺ T cells per 100 cells within a FL follicle (by IHC) were correlated with CD4 gene expression (normalized for the CCF) in 15 primary FL.
- (G) Correlation of CTSS and CD4 gene expression.
- (H) CD4/CD8 ratios of CTSS^{WT+low} FL versus CTSS^{Y132D/hi} FL or CTSS^{hi} FL or CTSS^{Y132D} FL. Additional comparisons are shown in Figures S6C–S6E; *p* value is from unpaired Student's *t* test.
- (I) Correlation of CTSS and PDL2 gene expression.
- (J) Progression of disease within 24 months (POD24) status of R-CHOP-treated patients with CTSS^{WT+low} FL (N = 33) versus CTSS^{Y132D/hi} FL (N = 16).
- (K) Kaplan-Meier plot for failure-free survival (FFS) of R-CHOP-treated patients with CTSS^{Y132D} FL (N = 6) plus CTSS^{hi} FL (N = 11) versus CTSS^{WT+low} (N = 34); *p* value is from log-rank test.

For all correlations the Pearson's *r* and the *p* value are indicated.

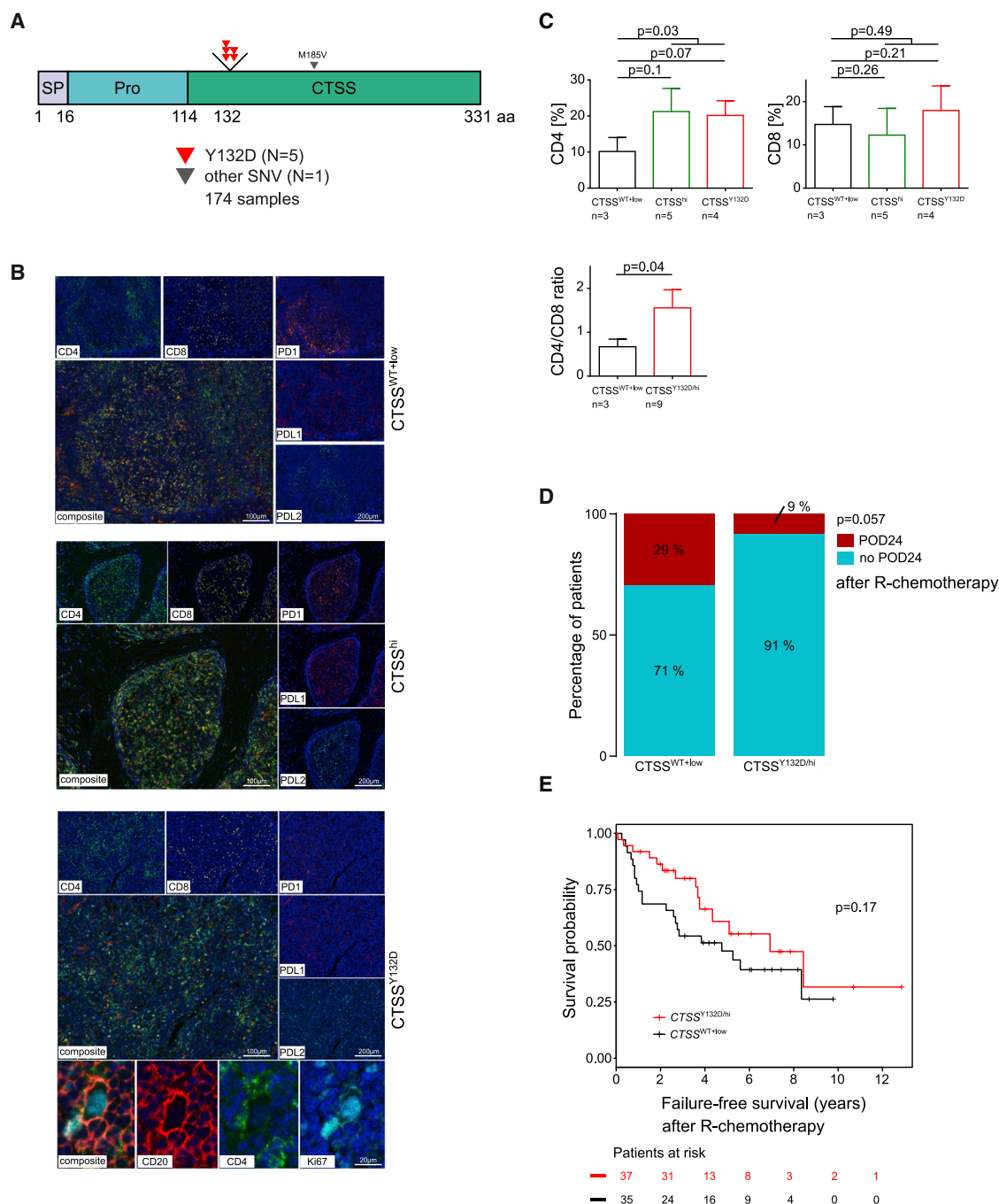


Figure 7. CTSS Hyperactivity in an Independent Validation Cohort

(A) CTSS mutation distribution and frequency in 174 primary FLs from a previously described cohort (Tobin et al., 2019). See also Table S3 for sequencing details. (B) Multispectral imaging of 3 representative FL biopsies; a minimum of $n = 3200$ cells were analyzed per patient; scale bars are 20, 100, or 200 μm as indicated. (C) Abundance of CD4⁺ and CD8⁺ T cells in 12 FL cases (CTSS^{WT+low} versus CTSS^{hi} versus CTSS^{Y132D}) and their CD4/CD8 ratio. See Figure S7 for correlations with selected immune genes (CD4, PDL2). Pooled data from biological replicates (n) are represented as mean \pm SEM; p values are from unpaired Student's t test. (D) POD24 status of R-chemotherapy (CHOP or CVP or bendamustine)-treated patients with CTSS^{WT+low} FL ($N = 56$) versus CTSS^{Y132D/hi} FL ($N = 13$); p value is from unpaired Student's t test. (E) Kaplan-Meier plot for FFS of patients with CTSS^{Y132D/hi} FL ($N = 37$) versus CTSS^{WT+low} FL ($N = 35$); p value is from log-rank test.

lymphomas that have undergone somatic hypermutation, characterized by T > G transversions at sites including ApTpN, matching the genomic context of Y132 in CTSS. However, we cannot exclude the possibility that CTSS^{Y132D} has additional gain-of-function effects providing a selective advantage over other Y132 and non-Y132 mutations that are not captured by our functional readouts.

Unlike other recurrent gene mutations involved in remodeling and co-opting the lymphoma immune microenvironment, such as *CREBBP* and *TNFRSF14*, we observe that mutations in CTSS are frequently subclonal. Also, the subsequent acquisition of distinct CTSS Y132 mutations after the formation of a common precursor clone in the case of donor-derived FLs is consistent with the hypothesis that these mutations often represent later events that contribute to FL progression and dissemination, rather than lymphoma formation.

As of today, to the best of our knowledge, CTSS Y132 mutations have only been identified in FL, including single cases within larger sequencing studies (Green et al., 2013; Morin et al., 2011). This may reflect underreporting, as few, if any, other targeted sequencing panels were designed to capture CTSS. However, CTSS activity can be aberrantly increased (i.e., hyperactivated) in FL and potentially in other lymphomas by alternative mechanisms. Here, we show that CTSS amplifications and CTSS Y132 mutations are mutually exclusive in FL. CTSS amplifications were associated with higher CTSS expression. In addition, transcriptional dysregulation of CTSS may be a more common finding in lymphoma and cancer in general; e.g., *BLIMP1/PRDM1* is frequently deleted in malignant lymphomas (Pasqualucci et al., 2006) and has been identified to function as a transcriptional repressor of CTSS (Kim et al., 2017).

Based on our functional *in vitro* and preclinical *in vivo* data, and supported by our findings in human FL, we propose a model in which aberrant CTSS hyperactivity induces and activates a CD4⁺ T cell enriched immune microenvironment that ultimately promotes tumor growth. Although the cellular adaptive immune system is often thought of in the context of immune surveillance and anti-tumor responses, the concept of CD4⁺ T cells supporting the growth of human FL cells actually dates back to the 1990s (Tsiagbe et al., 1993; Umetsu et al., 1990). The underlying immunological mechanisms, however, remain unclear. Additional functional studies in representative *in vivo* models, including immune cell depletion experiments, are required to capture the full scope of direct and indirect effects of aberrant CTSS hyperactivity on the complex interactions with various components of the immune microenvironment. However, mouse models may not always accurately reflect human conditions; e.g., in mice, CXCL13, a potent B cell chemoattractant and key regulator of lymphoid tissues (van de Pavert et al., 2009) is expressed by stromal cells. In humans, however, CXCL13 is produced at high levels by PD1⁺ GC CD4⁺ T_{FH} cells (Crotty, 2011). In fact, we identified CXCL13 to be among the most upregulated cytokines in human CTSS Y132 mutant FL. Thus, high CXCL13 levels in human FL may be the sequela of increased CD4⁺ T cell activation induced by aberrant CTSS hyperactivity. Conceptually, we hypothesize that even subclonal populations might be capable of eliciting this tumor-promoting immune phenotype, which could be amplified within the micro-

environment and substantially impact the biology and clinical course of the disease.

Importantly, our data indicate that the reprogrammed microenvironment in CTSS-hyperactive lymphomas is particularly sensitive to standard immunochemotherapy. Specifically, we show that patients with CTSS-hyperactive FL receiving standard immunochemotherapy (consisting of cytotoxic—in fact immuno-suppressive—chemotherapy, prednisone, and anti-CD20 antibodies) have lower rates of early treatment failure in two independent clinical cohorts. Although more in-depth analyses of larger cohorts of primary patient samples are needed, our observation nicely matches recent data: high immune cell infiltration (Tobin et al., 2019) and high intrafollicular CD4⁺ T cell abundance (Mondello et al., 2019) are consistently associated with more favorable treatment outcomes among patients with FL treated with immunochemotherapy. Our data provide a mechanistic explanation of these findings. This paradigm is different from other diseases, in which T cell infiltration can be harnessed (e.g., through immune checkpoint blockade) to drive an anti-tumor response. Here, the CD4⁺ T cell enriched immune microenvironment is promoting tumor growth. We propose that immunosuppressive immunochemotherapy functions by both directly killing lymphoma cells and disrupting the tumor-promoting immune microenvironment that CTSS-hyperactive FL have induced and particularly dependent on.

The impact of this paradigm, in which tumor-infiltrating T cells promote cancer growth, has not been adequately explored in other lymphomas or cancers. Thus, our work provides a strong rationale for future studies, e.g., to test whether other therapeutics (such as immune-modulatory drugs like lenalidomide) are also more effective in lymphomas dependent on infiltrating T cells and whether CTSS hyperactivity (or other markers of T cell infiltration) can be used as a predictive biomarker. Finally, future research should focus on the therapeutic utility of specific cathepsin inhibitors and explore CTSS-specific vulnerabilities and resistance phenotypes.

STAR★METHODS

Detailed methods are provided in the online version of this paper and include the following:

- KEY RESOURCES TABLE
- LEAD CONTACT AND MATERIALS AVAILABILITY
- EXPERIMENTAL MODEL AND SUBJECT DETAILS
 - Cell lines and mice
 - Patient information
- METHOD DETAILS
 - Plasmid construction
 - CRISPR/Cas9 strategy
 - sgRNAs and Cas9 plasmid design
 - ssDNA repair template design
 - Establishing CTSS Y132D mutant (CTSS^{Y132D}) and CTSS knock-out (CTSS^{KO}) cell lines
 - Quantitative real-time PCR analysis
 - PCR and Sanger sequencing of CTSS
 - Immunoblotting
 - Immunoprecipitation

- CTSS activity assay
- *In vitro* pro-CTSS autocatalytic assay
- Preparation of pro-, int-, and active CTSS WT for proteomic analysis
- Antigen processing and presentation assays
- CTSS epitope prediction
- Tumor inoculation and animal studies
- Tumor isolation
- Flow cytometry
- Mouse tumor immune assay (Luminex®100/200 System)
- Immunohistochemistry (IHC)
- Multispectral imaging analysis (Vectra® Polaris System)
- Profiling of the immune microenvironment
- Computational methods for molecular dynamics
- LC-MS/MS data acquisition
- LC-MS/MS database searching
- LC-MS/MS data analysis and visualization
- CTSS copy number detection in patient samples
- **QUANTIFICATION AND STATISTICAL ANALYSIS**
- **DATA AND CODE AVAILABILITY**

SUPPLEMENTAL INFORMATION

Supplemental Information can be found online at <https://doi.org/10.1016/j.celrep.2020.107522>.

ACKNOWLEDGMENTS

This work was funded by the Deutsche Forschungsgemeinschaft (DFG, German Research Foundation) project no. 360372040-SFB1335 (P04, principal investigator [PI] O.W.; P05, PI M.S.-S.) and project no. 278529602-SFB1243 (A11, PI O.W.; A12, PI M.S.-S.; A01, PI H.L.; A10, PI K.-P.H.). O.W. is funded by the Max-Eder program of the German Cancer Aid (#70112997). S.B. gratefully acknowledges the SPP1623 for funding. M.D.B. gratefully acknowledges the International Max Planck Research School for Molecular Life Sciences (IMPRS-LS).

We thank Bianka Ksienzyk (Laboratory for Leukemia Diagnostics, University Hospital, LMU) and Dr. Lisa Richter (Core Facility Flow Cytometry [CFFlow-Cyt], Biomedical Center [BMC], LMU) for help with cell sorting. Moreover, we thank Guido Piontek for help with multispectral imaging. Finally, we thank Prof. Ron Levy and Dr. Idit Sagiv-Barfi (Stanford Medicine) for helpful discussions regarding the A20/BALB/c mouse model.

AUTHOR CONTRIBUTIONS

D.B. designed and performed experiments, analyzed and interpreted experimental data, and wrote the initial manuscript draft; J.A.H. designed and performed experiments, analyzed and interpreted experimental and clinical data, and wrote the manuscript; S.S. performed experiments, performed CRISPR-Cas9 gene editing procedures, and analyzed and interpreted experimental data; S.H. performed experiments and analyzed and interpreted experimental and clinical data; S.A. analyzed and interpreted experimental and clinical data; C.P.T. performed mouse experiments; F.O.-B. performed experiments and did fluorescence-activated cell sorting (FACS) analysis; M.D.B. designed and performed CRISPR-Cas9 gene editing procedures; M.M. performed experiments; A.P. performed gene expression analysis; E.G. performed and analyzed chromosome genomic array testing; M.H. performed experiments; V.J. performed statistical analyses; K.R. performed Luminex experiments; J.G. performed experiments; M.B.S. performed experiments; M.S. performed gene expression experiments; J.R. performed IHC; W.K. provided patient samples and performed gene expression analysis and IHC; A.L.

performed experiments; C.L. performed mass-spectrometry-based proteomic analysis; S.B. designed and assisted with CRISPR-Cas9 gene editing procedures; H.L. oversaw CRISPR-Cas9 gene editing procedures; S.E. oversaw biochemical and structural experiments; K.-P.H. oversaw biochemical and structural experiments; W.H. interpreted experimental and clinical data; M.v.B.-B. interpreted experimental and clinical data; C.S. provided patient samples; R.K. interpreted experimental and clinical data; J.W.D.T. provided patient material; M.K.G. provided patient material; D.M.W. interpreted experimental and clinical data and wrote the manuscript; M.S.-S. designed experiments and interpreted experimental data; M.B.S. performed computational modeling; M.R. performed multispectral imaging; V.P. conducted bioinformatics and analysis and interpretation of experimental and clinical data; J.M. designed, planned, performed, and oversaw co-culture experiments; O.W. designed, planned, and oversaw all experiments; was involved in all aspects of analyzing and interpreting experimental and clinical data; and wrote the manuscript.

DECLARATION OF INTERESTS

The authors declare no competing interests.

Received: July 29, 2019

Revised: February 10, 2020

Accepted: March 26, 2020

Published: April 23, 2020

REFERENCES

- Adhikary, D., Behrends, U., Boerschmann, H., Pfänder, A., Burdach, S., Moosmann, A., Witter, K., Bornkamm, G.W., and Mautner, J. (2007). Immunodominance of lytic cycle antigens in Epstein-Barr virus-specific CD4+ T cell preparations for therapy. *PLoS One* 2, e583.
- Alexandrov, L.B., Nik-Zainal, S., Wedge, D.C., Aparicio, S.A., Behjati, S., Biankin, A.V., Bignell, G.R., Bolli, N., Borg, A., Børresen-Dale, A.L., et al.; Australian Pancreatic Cancer Genome Initiative; ICGC Breast Cancer Consortium; ICGC MML-Seq Consortium; ICGC PedBrain (2013). Signatures of mutational processes in human cancer. *Nature* 500, 415–421.
- Anderson, M.S., and Miller, J. (1992). Invariant chain can function as a chaperone protein for class II major histocompatibility complex molecules. *Proc. Natl. Acad. Sci. USA* 89, 2282–2286.
- Bararia, D., Kwok, H.S., Welner, R.S., Numata, A., Sárosi, M.B., Yang, H., Wee, S., Tschuri, S., Ray, D., Weigert, O., et al. (2016). Acetylation of C/EBP α inhibits its granulopoietic function. *Nat. Commun.* 7, 10968.
- Binnewies, M., Roberts, E.W., Kersten, K., Chan, V., Fearon, D.F., Merad, M., Coussens, L.M., Gabrilovich, D.I., Ostrand-Rosenberg, S., Hedrick, C.C., et al. (2018). Understanding the tumor immune microenvironment (TIME) for effective therapy. *Nat. Med.* 24, 541–550.
- Boice, M., Salloum, D., Mourcin, F., Sanghvi, V., Amin, R., Oricchio, E., Jiang, M., Mottok, A., Denis-Lagache, N., Ciriello, G., et al. (2016). Loss of the HVEM Tumor Suppressor in Lymphoma and Restoration by Modified CAR-T Cells. *Cell* 167, 405–418.e413.
- Bornkamm, G.W., Berens, C., Kuklik-Roos, C., Bechet, J.M., Laux, G., Bachl, J., Korndorfer, M., Schlee, M., Holzel, M., Malamoussi, A., et al. (2005). Stringent doxycycline-dependent control of gene activities using an episomal one-vector system. *Nucleic Acids Res* 33, e137.
- Carter, S.L., Cibulskis, K., Helman, E., McKenna, A., Shen, H., Zack, T., Laird, P.W., Onofrio, R.C., Winckler, W., Weir, B.A., et al. (2012). Absolute quantification of somatic DNA alterations in human cancer. *Nat. Biotechnol.* 30, 413–421.
- Challa-Malladi, M., Lieu, Y.K., Califano, O., Holmes, A.B., Bhagat, G., Murty, V.V., Dominguez-Sola, D., Pasqualucci, L., and Dalla-Favera, R. (2011). Combined genetic inactivation of β 2-Microglobulin and CD58 reveals frequent escape from immune recognition in diffuse large B cell lymphoma. *Cancer Cell* 20, 728–740.

- Cox, J., Neuhauser, N., Michalski, A., Scheltema, R.A., Olsen, J.V., and Mann, M. (2011). Andromeda: a peptide search engine integrated into the MaxQuant environment. *J. Proteome Res.* **10**, 1794–1805.
- Crotty, S. (2011). Follicular helper CD4 T cells (TFH). *Annu. Rev. Immunol.* **29**, 621–663.
- Dave, S.S., Wright, G., Tan, B., Rosenwald, A., Gascoyne, R.D., Chan, W.C., Fisher, R.I., Braziel, R.M., Rimsza, L.M., Grogan, T.M., et al. (2004). Prediction of survival in follicular lymphoma based on molecular features of tumor-infiltrating immune cells. *N. Engl. J. Med.* **351**, 2159–2169.
- Dunbrack, R.L., Jr. (2002). Rotamer libraries in the 21st century. *Curr. Opin. Struct. Biol.* **12**, 431–440.
- Ennishi, D., Takata, K., Béguélin, W., Duns, G., Mottok, A., Farinha, P., Basha-shati, A., Saberi, S., Boyle, M., Meissner, B., et al. (2019). Molecular and Genetic Characterization of MHC Deficiency Identifies EZH2 as Therapeutic Target for Enhancing Immune Recognition. *Cancer Discov.* **9**, 546–563.
- Erez, E., Fass, D., and Bibi, E. (2009). How intramembrane proteases bury hydrolytic reactions in the membrane. *Nature* **459**, 371–378.
- Fiebigler, B.M., Moosmann, A., Behrends, U., and Mautner, J. (2012). Mature proteins derived from Epstein-Barr virus fail to feed into the MHC class I antigenic pool. *Eur. J. Immunol.* **42**, 3167–3173.
- Gao, J., Aksoy, B.A., Dogrusoz, U., Dresdner, G., Gross, B., Sumer, S.O., Sun, Y., Jacobsen, A., Sinha, R., Larsson, E., et al. (2013). Integrative analysis of complex cancer genomics and clinical profiles using the cBioPortal. *Sci. Signal.* **6**, pii.
- Glas, A.M., Knoops, L., Delahaye, L., Kersten, M.J., Kibbelaar, R.E., Wessels, L.A., van Laar, R., van Krieken, J.H., Baars, J.W., Raemaekers, J., et al. (2007). Gene-expression and immunohistochemical study of specific T-cell subsets and accessory cell types in the transformation and prognosis of follicular lymphoma. *J. Clin. Oncol.* **25**, 390–398.
- Götz, A.W., Williamson, M.J., Xu, D., Poole, D., Le Grand, S., and Walker, R.C. (2012). Routine Microsecond Molecular Dynamics Simulations with AMBER on GPUs. 1. Generalized Born. *J. Chem. Theory Comput.* **8**, 1542–1555.
- Green, M.L., Leisenring, W.M., Xie, H., Walter, R.B., Mielcarek, M., Sandmaier, B.M., Riddell, S.R., and Boeckh, M. (2013). CMV reactivation after allogeneic HCT and relapse risk: evidence for early protection in acute myeloid leukemia. *Blood* **122**, 1316–1324.
- Green, M.R., Kihira, S., Liu, C.L., Nair, R.V., Salari, R., Gentles, A.J., Irish, J., Stehr, H., Vicente-Dueñas, C., Romero-Camarero, I., et al. (2015). Mutations in early follicular lymphoma progenitors are associated with suppressed antigen presentation. *Proc. Natl. Acad. Sci. USA* **112**, E1116–E1125.
- Hellmuth, J.C., Louissaint, A., Jr., Szczepanowski, M., Haebe, S., Pastore, A., Alig, S., Staiger, A.M., Hartmann, S., Kridel, R., Ducar, M.D., et al. (2018). Duodenal-type and nodal follicular lymphomas differ by their immune microenvironment rather than their mutation profiles. *Blood* **132**, 1695–1702.
- Huet, S., Tesson, B., Jais, J.P., Feldman, A.L., Magnano, L., Thomas, E., Traverse-Glehen, A., Albaud, B., Carrère, M., Xerri, L., et al. (2018). A gene-expression profiling score for prediction of outcome in patients with follicular lymphoma: a retrospective training and validation analysis in three international cohorts. *Lancet Oncol.* **19**, 549–561.
- Izadi, S., and Onufriev, A.V. (2016). Accuracy limit of rigid 3-point water models. *J. Chem. Phys.* **145**, 074501.
- Jiang, Y., Ortega-Molina, A., Geng, H., Ying, H.Y., Hatzl, K., Parsa, S., McNally, D., Wang, L., Doane, A.S., Agirre, X., et al. (2017). CREBBP Inactivation Promotes the Development of HDAC3-Dependent Lymphomas. *Cancer Discov.* **7**, 38–53.
- Jurinovic, V., Kridel, R., Staiger, A.M., Szczepanowski, M., Horn, H., Dreyling, M.H., Rosenwald, A., Ott, G., Klapper, W., Zelenetz, A.D., et al. (2016). Clinico-genetic risk models predict early progression of follicular lymphoma after first-line immunochemotherapy. *Blood* **128**, 1112–1120.
- Kaulmann, G., Palm, G.J., Schilling, K., Hilgenfeld, R., and Wiederanders, B. (2006). The crystal structure of a Cys25 → Ala mutant of human procathepsin S elucidates enzyme-prosequence interactions. *Protein Sci.* **15**, 2619–2629.
- Kiaii, S., Clear, A.J., Ramsay, A.G., Davies, D., Sangaralingam, A., Lee, A., Calaminici, M., Neuberger, D.S., and Gribben, J.G. (2013). Follicular lymphoma cells induce changes in T-cell gene expression and function: potential impact on survival and risk of transformation. *J. Clin. Oncol.* **31**, 2654–2661.
- Kim, K.J., Kanellopoulos-Langevin, C., Merwin, R.M., Sachs, D.H., and Asofsky, R. (1979). Establishment and characterization of BALB/c lymphoma lines with B cell properties. *J. Immunol.* **122**, 549–554.
- Kim, S.J., Schätzle, S., Ahmed, S.S., Haap, W., Jang, S.H., Gregersen, P.K., Georgiou, G., and Diamond, B. (2017). Increased cathepsin S in Prdm1^{−/−} dendritic cells alters the T_{FH} cell repertoire and contributes to lupus. *Nat. Immunol.* **18**, 1016–1024.
- Koues, O.I., Kowalewski, R.A., Chang, L.W., Pyfrom, S.C., Schmidt, J.A., Luo, H., Sandoval, L.E., Hughes, T.B., Bednarski, J.J., Cashen, A.F., et al. (2015). Enhancer sequence variants and transcription-factor deregulation synergize to construct pathogenic regulatory circuits in B-cell lymphoma. *Immunity* **42**, 186–198.
- Maier, J.A., Martinez, C., Kasavajhala, K., Wickstrom, L., Hauser, K.E., and Simmerling, C. (2015). ff14SB: Improving the Accuracy of Protein Side Chain and Backbone Parameters from ff99SB. *J. Chem. Theory Comput.* **11**, 3696–3713.
- McGrath, M.E., Palmer, J.T., Brömmle, D., and Somoza, J.R. (1998). Crystal structure of human cathepsin S. *Protein Sci.* **7**, 1294–1302.
- Mondello, P., Fama, A., Larson, M.C., Yang, Z., Villaboas, J.C., Feldman, A.L., Slager, S.L., Link, B.K., Syrbu, S., Novak, A.J., et al. (2019). Intrafollicular CD4⁺ T-Cells As an Independent Predictor of Early Clinical Failure in Newly Diagnosed Follicular Lymphoma. *Blood* **134**, 121.
- Morin, R.D., Mendez-Lago, M., Mungall, A.J., Goya, R., Mungall, K.L., Corbett, R.D., Johnson, N.A., Severson, T.M., Chiu, R., Field, M., et al. (2011). Frequent mutation of histone-modifying genes in non-Hodgkin lymphoma. *Nature* **476**, 298–303.
- Mulholland, C.B., Smets, M., Schmidtman, E., Leidescher, S., Markaki, Y., Hofweber, M., Qin, W., Manzo, M., Kremmer, E., Thanisch, K., et al. (2015). A modular open platform for systematic functional studies under physiological conditions. *Nucleic Acids Res.* **43**, e112.
- O'Shea, D., O'Riain, C., Taylor, C., Waters, R., Carlotti, E., Macdougall, F., Gribben, J., Rosenwald, A., Ott, G., Rimsza, L.M., et al. (2008). The presence of TP53 mutation at diagnosis of follicular lymphoma identifies a high-risk group of patients with shortened time to disease progression and poorer overall survival. *Blood* **112**, 3126–3129.
- Olson, O.C., and Joyce, J.A. (2015). Cysteine cathepsin proteases: regulators of cancer progression and therapeutic response. *Nat. Rev. Cancer* **15**, 712–729.
- Pasqualucci, L., Compagno, M., Houldsworth, J., Monti, S., Grunn, A., Nandula, S.V., Aster, J.C., Murty, V.V., Shipp, M.A., and Dalla-Favera, R. (2006). Inactivation of the PRDM1/BLIMP1 gene in diffuse large B cell lymphoma. *J. Exp. Med.* **203**, 311–317.
- Pastore, A., Jurinovic, V., Kridel, R., Hoster, E., Staiger, A.M., Szczepanowski, M., Pott, C., Kopp, N., Murakami, M., Horn, H., et al. (2015). Integration of gene mutations in risk prognostication for patients receiving first-line immunochemotherapy for follicular lymphoma: a retrospective analysis of a prospective clinical trial and validation in a population-based registry. *Lancet Oncol.* **16**, 1111–1122.
- Petersen, E.F., Goddard, T.D., Huang, C.C., Couch, G.S., Greenblatt, D.M., Meng, E.C., and Ferrin, T.E. (2004). UCSF Chimera—a visualization system for exploratory research and analysis. *J. Comput. Chem.* **25**, 1605–1612.
- Quraishi, O., and Storer, A.C. (2001). Identification of internal autolytic cleavage sites within the prosegments of recombinant procathepsin B and procathepsin S. Contribution of a plausible unimolecular autolytic event for the processing of zymogens belonging to the papain family. *J. Biol. Chem.* **276**, 8118–8124.
- Ran, F.A., Hsu, P.D., Wright, J., Agarwala, V., Scott, D.A., and Zhang, F. (2013). Genome engineering using the CRISPR-Cas9 system. *Nat. Protoc.* **8**, 2281–2308.

- Rao, P.H., Houldsworth, J., Dyomina, K., Parsa, N.Z., Cigudosa, J.C., Louie, D.C., Popplewell, L., Offit, K., Jhanwar, S.C., and Chaganti, R.S. (1998). Chromosomal and gene amplification in diffuse large B-cell lymphoma. *Blood* 92, 234–240.
- Riese, R.J., Wolf, P.R., Brömme, D., Natkin, L.R., Villadangos, J.A., Ploegh, H.L., and Chapman, H.A. (1996). Essential role for cathepsin S in MHC class II-associated invariant chain processing and peptide loading. *Immunity* 4, 357–366.
- Rückrich, T., Brandenburg, J., Cansier, A., Müller, M., Stevanović, S., Schilling, K., Wiederanders, B., Beck, A., Melms, A., Reich, M., et al. (2006). Specificity of human cathepsin S determined by processing of peptide substrates and MHC class II-associated invariant chain. *Biol. Chem.* 387, 1503–1511.
- Sali, A., and Blundell, T.L. (1993). Comparative protein modelling by satisfaction of spatial restraints. *J. Mol. Biol.* 234, 779–815.
- Salomon-Ferrer, R., Götz, A.W., Poole, D., Le Grand, S., and Walker, R.C. (2013). Routine Microsecond Molecular Dynamics Simulations with AMBER on GPUs. 2. Explicit Solvent Particle Mesh Ewald. *J. Chem. Theory Comput.* 9, 3878–3888.
- Schneider, C.A., Rasband, W.S., and Eliceiri, K.W. (2012). NIH Image to ImageJ: 25 years of image analysis. *Nat. Methods* 9, 671–675.
- Scott, D.W., and Gascoyne, R.D. (2014). The tumour microenvironment in B cell lymphomas. *Nat. Rev. Cancer* 14, 517–534.
- Sevenich, L., Bowman, R.L., Mason, S.D., Quail, D.F., Rapaport, F., Elie, B.T., Brogi, E., Brastianos, P.K., Hahn, W.C., Holsinger, L.J., et al. (2014). Analysis of tumour- and stroma-supplied proteolytic networks reveals a brain-metastasis-promoting role for cathepsin S. *Nat. Cell Biol.* 16, 876–888.
- Shapovalov, M.V., and Dunbrack, R.L., Jr. (2011). A smoothed backbone-dependent rotamer library for proteins derived from adaptive kernel density estimates and regressions. *Structure* 19, 844–858.
- Shen, L., Sigal, L.J., Boes, M., and Rock, K.L. (2004). Important role of cathepsin S in generating peptides for TAP-independent MHC class I cross-presentation in vivo. *Immunity* 21, 155–165.
- Shevchenko, A., Tomas, H., Havlis, J., Olsen, J.V., and Mann, M. (2006). In-gel digestion for mass spectrometric characterization of proteins and proteomes. *Nat. Protoc.* 1, 2856–2860.
- Swerdlow, S.H., Campo, E., Pileri, S.A., Harris, N.L., Stein, H., Siebert, R., Advani, R., Ghielmini, M., Salles, G.A., Zelenetz, A.D., and Jaffe, E.S. (2016). The 2016 revision of the World Health Organization classification of lymphoid neoplasms. *Blood* 127, 2375–2390.
- Talevich, E., Shain, A.H., Botton, T., and Bastian, B.C. (2016). CNVkit: Genome-Wide Copy Number Detection and Visualization from Targeted DNA Sequencing. *PLoS Comput. Biol.* 12, e1004873.
- Tobin, J.W.D., Keane, C., Gunawardana, J., Mollee, P., Birch, S., Hoang, T., Lee, J., Li, L., Huang, L., Murigneux, V., et al. (2019). Progression of Disease Within 24 Months in Follicular Lymphoma Is Associated With Reduced Intratumoral Immune Infiltration. *J. Clin. Oncol.* 37, 3300–3309.
- Tsiagbe, V.K., Asakawa, J., Miranda, A., Sutherland, R.M., Paterson, Y., and Thorbecke, G.J. (1993). Syngeneic response to SJL follicular center B cell lymphoma (reticular cell sarcoma) cells is primarily in V beta 16+ CD4+ T cells. *J. Immunol.* 150, 5519–5528.
- Tyanova, S., Temu, T., and Cox, J. (2016). The MaxQuant computational platform for mass spectrometry-based shotgun proteomics. *Nat. Protoc.* 11, 2301–2319.
- Umetsu, D.T., Esserman, L., Donlon, T.A., DeKruyff, R.H., and Levy, R. (1990). Induction of proliferation of human follicular (B type) lymphoma cells by cognate interaction with CD4+ T cell clones. *J. Immunol.* 144, 2550–2557.
- Untergasser, A., Nijveen, H., Rao, X., Bisseling, T., Geurts, R., and Leunissen, J.A. (2007). Primer3Plus, an enhanced web interface to Primer3. *Nucleic Acids Res.* 35, W71–W74.
- van de Pavert, S.A., Olivier, B.J., Govers, G., Vondenhoff, M.F., Greuter, M., Beke, P., Kusser, K., Höpken, U.E., Lipp, M., Niederreither, K., et al. (2009). Chemokine CXCL13 is essential for lymph node initiation and is induced by retinoic acid and neuronal stimulation. *Nat. Immunol.* 10, 1193–1199.
- Vasiljeva, O., Dolinar, M., Pungercar, J.R., Turk, V., and Turk, B. (2005). Recombinant human procathepsin S is capable of autocatalytic processing at neutral pH in the presence of glycosaminoglycans. *FEBS Lett.* 579, 1285–1290.
- Weigert, O., and Weinstock, D.M. (2017). The promises and challenges of using gene mutations for patient stratification in follicular lymphoma. *Blood* 130, 1491–1498.
- Weigert, O., Kopp, N., Lane, A.A., Yoda, A., Dahlberg, S.E., Neuberg, D., Bahar, A.Y., Chapuy, B., Kutok, J.L., Longtine, J.A., et al. (2012). Molecular ontogeny of donor-derived follicular lymphomas occurring after hematopoietic cell transplantation. *Cancer Discov.* 2, 47–55.
- Yam, C.S., and Hajjar, A.M. (2013). Whole Spleen Flow Cytometry Assay. *Biol. Protoc.* 3, e834.
- Zhang, J., Vlasevska, S., Wells, V.A., Nataraj, S., Holmes, A.B., Duval, R., Meyer, S.N., Mo, T., Basso, K., Brindle, P.K., et al. (2017). The CREBBP Acetyltransferase Is a Haploinsufficient Tumor Suppressor in B-cell Lymphoma. *Cancer Discov.* 7, 322–337.

STAR★METHODS

KEY RESOURCES TABLE

REAGENT or RESOURCE	SOURCE	IDENTIFIER
Bacterial and Virus Strains		
pHAGE CMV MCS-IRES-ZsGreen	Harvard plasmid repository Clone ID	EvNO00061605
pHAGE CMV MCS-IRES-ZsGreen CTSS WT	This paper	N/A
pHAGE CMV MCS-IRES-ZsGreen CTSS M185V	This paper	N/A
pHAGE CMV MCS-IRES-ZsGreen CTSS Y132D	This paper	N/A
pHAGE CMV MCS-IRES-ZsGreen CTSS Y132S	This paper	N/A
pMSCV-IRES-GFP	Addgene	Addgene #52107
pMSCV-IRES-GFP CTSS WT	This paper	N/A
pMSCV-IRES-GFP CTSS Y132D	This paper	N/A
Biological Samples		
Primary patient samples (GLSG2000, BCCA cohort)	Weigert et al., 2012 ; Pastore et al., 2015	N/A
Primary patient samples (discovery cohort)	Tobin et al., 2019	N/A
Chemicals, Peptides, and Recombinant Proteins		
Anti-FLAG® M2 Magnetic Beads	Sigma	Cat# M8823, RRID:AB_2637089
BBLF1 (aa ₂₂₋₃₆ -GGIINLYNDYEEFNL-)	N/A	N/A
BHRF1 (aa ₁₆₁₋₁₇₅ -SRRFSWTLFLAGLTL-)	N/A	N/A
BMLF1 (aa ₂₅₉₋₂₆₇ -GLCTLVAML-)	N/A	N/A
BZLF1 (aa ₁₉₀₋₁₉₇ -RAKFKQLL-)	N/A	N/A
BZLF1 (aa ₁₇₄₋₁₈₈ -ELEIKRYKNRVASRK-)	N/A	N/A
E-64	Sigma	E3132
EBNA-LP (aa ₄₃₋₅₅ -RRVRRRLVQQEE-)	N/A	N/A
Nucleofector™ Solution V	Lonza	Cat# VVCA-1003
Protein G agarose beads	Sigma	11719416001
TRIZOL	ThermoFisher Scientific	Cat# 15596026
Trypsin Gold Mass spectrometry grade	Promega	Cat# V528A
Critical Commercial Assays		
Cathepsin S Activity Fluorometric Assay Kit	BioVision	Cat# K144
CTSS TaqMan® Gene Expression Assays	ThermoFisher Scientific	Hs00175407_m1 CTSS and Hs99999907_m1 B2M
ExpressArt FFPE Clear RNAREady kit	AmpTec	Cat# 9009-A100
Gateway Vector Conversion System	ThermoFisher Scientific	Cat# 11828029
nCounter PanCancer Immune Profiling Panel	NanoString	N/A
Oncoscan® CNVkit	Affymetrix	Cat# 902293
SuperScript® III First-Strand Synthesis System for RT-PCR	Invitrogen	Cat# 18080-051

(Continued on next page)

Continued

REAGENT or RESOURCE	SOURCE	IDENTIFIER
Deposited Data		
CTSS structure	Protein Data Bank	PDB:2C0Y
Gene expression data (GLSG2000 and BCCA)	Gene Expression Omnibus (GEO) repository	GEO: GSE66166
Gene expression data of malignant versus non-malignant cells	GEO	GEO: GSE62246
Gene expression data (training cohort)	GEO	GEO: GSE147125
Gene expression data (validation cohort)	GEO	GEO: GSE147033
Proteomics data	ProteomeXchange Consortium (http://proteomecentral.proteomexchange.org)	PRIDE: PXD014612
Raw data for main figures	Mendeley Data	Mendeley Data: https://doi.org/10.17632/pr5cfx8mnh.1
Experimental Models: Cell Lines		
Human: DG75	ATCC	Cat# CRL-2625, RRID:CVCL_0244
Human: HEK293T	ATCC	Cat# CRL-11268, RRID:CVCL_1926
Human: Karpas 422	Ximbio	Cat# 152419, RRID:CVCL_1325
Human: T cell clones 3#1	N/A	N/A
Human: T cell clones HDe	N/A	N/A
Human: T cell clones GBW3#5	N/A	N/A
Human: T cell clones #P11	N/A	N/A
Human: T cell clones F#4	N/A	N/A
Human: T cell clones GLC#7	N/A	N/A
Human: T cell clones 3H11	N/A	N/A
Mouse: A20	ATCC	ATCC Cat# TIB-208, RRID:CVCL_1940
Mouse Model		
Mouse: BALB/c	Jackson Laboratory	000651
Oligonucleotides		
See Table S1		N/A
Recombinant DNA		
CTSS (Homo sapiens) in pDONR201 (Gateway donor/master vector)	Dnasu plasmid repository Clone ID	HsCD00005390
pcDNA6/TR vector Mammalian Expression Vector	ThermoFisher Scientific	Cat# V102520
pTet EBO-GFP Mammalian Expression Vector	Bornkamm et al., 2005	N/A
pHAGE CMV MCS-IRES-ZsGreen	Harvard plasmid repository Clone ID	EvNO00061605
pMSCV-IRES-GFP	Addgene	Addgene 52107
pSpCas9(BB)-2A-GFP	Addgene	RRID:Addgene_48138
Software and Algorithms		
AmberTools17 and AMBER12 packages	AMBER	http://ambermd.org
Biorender	Biorender	https://biorender.com
CNVkit	CNVkit 0.9.5	https://github.com/etal/cnvkit
Dunbrack library	Shapovalov and Dunbrack, 2011	http://dunbrack.fccc.edu/
GraphPad Prism 6.07	GraphPad	https://www.graphpad.com
ImageJ	Schneider et al., 2012	https://imagej.net/Fiji
Inkscape 0.92	Inkscape	https://www.inkscape.org
MaxQuant (version 1.6.3.4)	Andromeda	https://www.maxquant.org/

(Continued on next page)

Continued

REAGENT or RESOURCE	SOURCE	IDENTIFIER
modeller	Sali and Blundell, 1993	https://salilab.org/modeller/
OncoPrinter	cBioPortal 3.0.2	https://www.cbioportal.org
OncoScan Console 1.3	Thermo Fisher Scientific	https://www.thermofisher.com/us/en/home.html
R Studio (1.1.463/R 3.6.0)	Packages:	https://www.r-project.org/
	pheatmap_1.0.12	
	DESeq2_1.24.0	
	gplots_3.0.1.1	
	survminer_0.4.4	
	ggpubr_0.2.1	
	survival_2.44-1.1	
	ggplot2_3.2.0	
	dplyr_0.8.3	
	beadarray_2.34.0	
	limma_3.40.2	
	rCGH_1.14.0	
UCSF Chimera	Pettersen et al., 2004	https://www.cgl.ucsf.edu/chimera/

LEAD CONTACT AND MATERIALS AVAILABILITY

Further information and requests for resources and reagents should be directed to and will be fulfilled by the Lead Contact, Oliver Weigert (oliver.weigert@med.uni-muenchen.de). All unique/stable reagents used or generated in this study will be made available on request.

EXPERIMENTAL MODEL AND SUBJECT DETAILS

Cell lines and mice

HEK293T (ATCC, CRL11268) cells were maintained in DMEM (Biowest) supplemented with 10% heat-inactivated FBS (Biowest). Karpas422 and DG75 were maintained in RPMI 1640 (gibco) supplemented with 10% heat-inactivated FBS. Doxycycline inducible cell lines were maintained in respective medium supplemented with 10% charcoal-stripped FBS (Invitrogen). A20 B cell lymphoma cells were cultured in RPMI 1640 with 10% FBS, 1 x Pen-strep (gibco), 25 mM HEPES (Pan-biotech), 1 x GlutaMax (gibco), 1 x MEM NEAA (gibco) and 50 μ M 2-mercaptoethanol (gibco). Karpas422 and HEK293T cell identities were confirmed by STR profiling. All cell lines are tested negative for mycoplasma contamination by MycoAlert PLUS mycoplasma detection kit (Lonza).

5-week-old female BALB/c were purchased from The Jackson Laboratory. Mice were housed in the Longwood Center Animal Facility of Dana Farber Cancer Institute (Boston, MA). All experiments were approved by the Harvard's administrative panel on laboratory animal care and conducted in accordance with the Animal Research Advisory Committee Guidelines.

Patient information

Patient tissue specimens were available from previously reported cohorts from the GLSG2000 trial and the BCCA registry ([Pastore et al., 2015](#)) and from another cohort that consisted of 174 patients with FL from a prospectively maintained clinical lymphoma database that had also been reported previously ([Tobin et al., 2019](#)).

A total of 51 patients from the GLSG2000 cohort used for Kaplan-Meier plots included 51% females (N = 26; mean age 55.0 years) and 49% males (N = 25; mean age 55.4 years). A total of 72 patients from the validation cohort ([Tobin et al., 2019](#)) used for Kaplan-Meier plots included 50% females (N = 36; mean age 58.8 years) and 50% males (N = 36; mean age 58.4 years).

All studies were approved by relevant institutional regulatory boards in concordance with the Declaration of Helsinki. All patients had signed informed consent which included molecular analyses.

METHOD DETAILS

Plasmid construction

A gateway cassette (Gateway - GW) was cloned into pHAGE CMV MCS-IRES-ZsGreen (pCIG GW; Harvard plasmid repository Clone ID: EvNO00061605) and pMSCV-IRES-GFP (pMIG GW; Addgene plasmid #20672) using the Gateway Vector Conversion System (ThermoFisher Scientific).

Human CTSS WT gateway donor entry vector (Harvard plasmid repository Clone ID: HsCD00005390) was used to introduce the Y132D mutation by site-directed mutagenesis using Phusion® High-Fidelity polymerase (New England Biolabs). CTSS WT and Y132D cDNA were cloned from pDONOR201 into different kinds of expression vectors (pCIG-GW, pMIG-GW and pcDNA6) using Gateway® cloning (ThermoFisher Scientific). An in-frame single FLAG tag between the signal peptide (SP) and the *pro*-CTSS sequence was inserted by PCR using pcDNA6 CTSS WT and Y132D mutant as template and cloned into a shuttle vector. pcDNA6 CTSS WT and Y132D were PCR amplified using pDONOR201 CTSS WT and Y132D as template and cloned into pcDNA6 EV using EcoRI and XhoI. Shuttle vectors containing either CTSS WT or Y132D inserts were *Sfi*I digested to sub-clone CTSS in a pTet EBO-GFP expression vector (Bornkamm et al., 2005), a bi-directional doxycycline (dox)-regulated promoter (GFP and the gene of interest). Insert sequences were confirmed by Sanger sequencing, using the oligos (CTSS_Foward and CTSS_Reverse) listed in Table S1.

CRISPR/Cas9 strategy

We used a homologous-recombination-mediated CRISPR/Cas9 strategy to introduce the Y132D mutation to the endogenous CTSS locus in the lymphoma cell line Karpas422 (details provided below). Two representative, single-cell derived clones - namely E2 and H41 - were used for subsequent experiments. Sanger sequencing of the targeted genomic locus and reverse transcription (RT)-PCR of CTSS exons 2-5 confirmed their biallelic Y132D knock-in identity (Figure S1A). The Karpas422 and DG75 CTSS^{KO} clones were generated by targeting the exon-intron boundary, resulting in a frameshift within the coding region, ultimately leading to premature termination of translation (Figure S1B). The mRNA of the DG75 CTSS^{KO} clone exhibited decreased stability (Figure S1C).

sgRNAs and Cas9 plasmid design

The sgRNAs were designed using the Benchling CRISPR design online tool ([Biology Software], accessed 2015, retrieved from <https://benchling.com/faq>). To establish CTSS Y132D mutant (CTSS^{Y132D}) or CTSS knock-out (CTSS^{KO}) cell lines the sgRNAs were cloned into plasmid pSpCas9(BB)-2A-GFP (PX458, a gift from Feng Zhang, Addgene plasmid #48138) as described elsewhere (Ran et al., 2013). Table S1 lists all oligo sequences that were cloned into pSpCas9(BB)-2A-GFP.

ssDNA repair template design

A 200 nt ssDNA repair template (4 nM Ultramer™ DNA Oligonucleotide, Standard Desalting, Integrated DNA Technologies) was designed with homology arms centered around the CTSS Y132D mutation. The CTSS Y132D mutation introduces a DpnII (New England Biolabs) restriction site to screen for positive recombination events. Re-cleavage of the endogenous locus after repair template incorporation was prevented by co-delivering a silent CRISPR/Cas9-blocking mutation within the respective PAM. The sequence of the 200 nt ssDNA repair template to generate the CTSS Y132D mutant is given in Table S1 (mutations are indicated in capital letters).

Establishing CTSS Y132D mutant (CTSS^{Y132D}) and CTSS knock-out (CTSS^{KO}) cell lines

1 × 10⁶ cells were transfected with pSpCas9(BB)-2A-GFP co-expressing the respective sgRNA using Nucleofector™ Solution V and the Nucleofector™2b according to manufacturer's instructions. 48 hours (hr) following transfection, GFP-positive cells were single cell sorted into 96-well plates. After 10-14 days, plates were screened for cell growth and clones individually collected on a 96-well plate. After cell outgrowth, 96-well plates were duplicated, and genomic DNA isolated for screening by PCR as previously described with minor modifications (Mulholland et al., 2015). Briefly, cells were washed two times with PBS, resuspended in 50 µL/well lysis buffer (50 mM TRIS/HCl pH 7.5, 10 mM CaCl₂, 1.7 µM SDS, 50 µg/mL Proteinase K), frozen at -80°C for 30 minutes (min), incubated at 56°C for 3 hr, and finally Proteinase K heat inactivated at 85°C for 30 min. 2.5 µL/well of the resulting crude cell lysate were directly subjected to PCR (25 µL/rxn, 0.1 µL MyTaq DNA Polymerase, Biorline) using the appropriate external screening primers below and following cycling settings: 95°C/5' - [95°C/30 s - 60°C/30 s - 72°C/30 s] × 45 - 72°C/40 s - 4°C/∞. To screen for CTSS Y132D mutants, 7.5 µL PCR products were digested overnight with DpnII (20 µL/rxn, 0.5 µL restriction enzyme, New England Biolabs).

Restriction fragments were subsequently analyzed on 1.5% agarose gels and homozygous clones identified by complete digest of PCR products. To screen for CTSS^{KO} (via mutation, deletions or insertion) by PCR, products were analyzed on 1.5% agarose gels. PCR products of positive clones were validated by Sanger sequencing (screening oligos are listed in Table S1). CTSS^{Y132D} cell lines were further tested by Sanger sequencing of CTSS cDNA and CTSS^{KO} clones were additionally confirmed by western blotting.

Quantitative real-time PCR analysis

RNA isolation was performed using TRIzol reagent (Ambion). RNA was isolated from Karpas422 native, Y132D knock-in, DG75 native and DG75 CTSS^{KO} cell lines. RNA was transcribed to cDNA using SuperScript® III First-Strand Synthesis System (ThermoFisher Scientific). Equal amounts of cDNA were used for all conditions, and gene expression was quantified by CTSS (Hs00175407_m1 CTSS) and housekeeping *B2M* (Hs99999907_m1 *B2M*) TaqMan assays using 7900HT Fast Real-Time PCR System (Applied Biosystems).

PCR and Sanger sequencing of CTSS

PCR primers were designed with Primer3 (Untergasser et al., 2007) and Sanger sequencing was performed at GATC Biotech.

Immunoblotting

For western blotting of whole-cell lysates, 1×10^7 cells were lysed with radio immunoprecipitation assay buffer (RIPA). Protein concentrations were quantitated with Pierce BCA assay (ThermoFisher scientific). Proteins were separated on 12% SDS-PAGE gels. Immunoblots were incubated with primary antibody overnight at 4°C, followed by a secondary horseradish peroxidase-conjugated antibody at room temperature for 1 hr. Antibodies used were: CTSS (Peptide: Q17-I331) Goat AF1183 R&D Systems WB (1:2000), FLAG-M2 Mouse F3165 Sigma-Aldrich WB (1:3000, for IP: 2 µg), HSP90 Mouse #4877 Cell Signaling WB (1:1000), CD74 Mouse Ab9514 Abcam WB (1:1000), β -tubulin Rabbit #2128 Cell Signaling WB (1:6000), Normal Goat IgG Control Goat #AB 108-C (2 µg), R&D Systems Rabbit-IgG-HRP Goat #31460 ThermoFisher Scientific WB (1:2000), Goat-IgG-HRP Donkey sc-2020 Santa Cruz WB (1:2000), Mouse-IgG-HRP Goat #31430 ThermoFisher Scientific WB (1:5000). See also [Table S2](#) for antibody details.

For CD74 western blotting E-64 (Sigma, E3132) cathepsin inhibitor (18 hr 7.5 µM for Karpas422, 36 hr 75 µM for DG75) was added before lysates were taken.

Band intensities of western blots were quantified using ImageJ densitometry and plotted in Prism 6.

Immunoprecipitation

For immunoprecipitation of CTSS using Karpas422 cells, 600 µg of whole cell lysate was used. Cell lysates were prepared using 1 x passive lysis buffer (PLB, Promega). 0.5 x PLB buffer diluted in d_2O was used as immunoprecipitation buffer. Lysates were pre-cleared with goat 2 µg IgG antibody (Cell Signaling Technology) and Protein G agarose beads (Sigma), while the CTSS antibody was bound to Protein G agarose beads for 1 hr at 4°C. Subsequently, the pre-cleared lysate was incubated with the bead-bound antibody for 2 hr with constant rotation at 4°C. Bead-bound immunoprecipitates were washed thrice with immunoprecipitation buffer. Immunoprecipitation of FLAG-tagged proteins with M2 agarose magnetic beads (Sigma) was performed according to manufacturer's instructions. Briefly, 10 mg of PLB lysed HEK293T cells were incubated with anti-FLAG M2 agarose beads in 0.5 x PLB buffer for 3 hr at 4°C. Bead-bound immunoprecipitates were washed once with 0.5 x PLB buffer containing 200 mM NaCl, once with 100 mM NaCl, once with immunoprecipitation buffer, followed by 50 mM Tris-Cl (pH 7.5). Proteins were eluted from the beads in the 50 mM Tris-Cl buffer with triple FLAG peptide (Sigma Aldrich) according to manufacturer instructions at 4°C for 1 hr with constant shaking. The eluent was analyzed with a silver stained gel and protein estimation was done according to diluted BSA (New England BioLabs).

CTSS activity assay

The CTSS substrate cleavage activity was measured in 100 µL reaction volume in a 96-well plate using Valine-Valine-Arginine labeled with amino-4-trifluoromethyl coumarin (Z-VVR-AFC) as a substrate (Cathepsin S Activity Fluorometric Assay Kit, BioVision, SF, USA) and the provided reaction buffer (pH 5.5) from the kit. The following enzymes were used for the assay: i) Immunoprecipitated CTSS from Karpas422 cells using the polyclonal CTSS antibody, ii) purified FLAG-tagged pro-CTSS from HEK293T using anti-FLAG magnetic beads iii) active CTSS enzyme resulting from purified pro-CTSS following 24 hr incubation in reaction buffer at 37°C. The active enzyme leads to hydrolysis of the substrate, resulting in the fluorescence of the AFC product which was measured with the Glomax® fluorometer (Promega) at an excitation wavelength of 400 nm and an emission wavelength of 505 nm. FF-FMK provided in the kit was used as a CTSS inhibitor in control wells.

In vitro pro-CTSS autocatalytic assay

Protein concentrations of eluted FLAG tagged protein were determined using Qubit and by silver stained SDS-PAGE using BSA as standards. Auto-processing of pro-CTSS was monitored at 37°C in 60 µL volume. A time-course experiment was set up for the indicated time-points (0–180 min) using highly purified pro-CTSS. Each reaction consisted of 38.5 µL of reaction buffer (pH 5.5 BioVision), 25 µg/mL dextran sulfate, and 100 ng of the respective pro-enzyme protein. Aliquots of 60 µL were taken out from the reaction mixture at the indicated time points (0, 15, 30, 45, 180 min), denatured by adding SDS sample buffer and boiling for 5 min at 90°C. Auto-processing was analyzed by silver stained 12% SDS-PAGE gel. Band intensities were quantified using ImageJ densitometry.

Preparation of pro-, int-, and active CTSS WT for proteomic analysis

Purified FLAG-tagged pro-CTSS^{WT} was incubated at 37°C in BioVision buffer in a total volume of 60 µL. Each reaction consisted of 36 µL of reaction buffer (pH 5.5 BioVision) and 20 µL (200 ng) pro-CTSS^{WT}. After 3 hr incubation all 3 CTSS forms (pro-, int-, and active CTSS) are present and samples were denatured by adding SDS sample buffer and boiling for 5 min at 90°C. Next, proteins were reduced with 50 mM DTT and alkylated with 55 mM CAA. Subsequent a 4%–12% SDS-PAGE gel electrophoresis separated CTSS in its 3 apparent forms. In total, 3 replicates of the pro-CTSS form, 4 replicates of the int-CTSS form and 4 replicates of the active CTSS form were prepared and investigated. The proteins on the gel were Coomassie stained using the ThermoFisher Scientific Pierce Power Stainer (Cat. No. 22833), bands were cut out and transferred to 1.5 mL Eppendorf tubes using the X-TRACTA (Biozym). In-gel trypsin digestion was performed according to standard procedures ([Shevchenko et al., 2006](#)).

Antigen processing and presentation assays

Native DG75 cells and the CTSS^{KO} clone 2A1 were grown as suspension cultures in complete RPMI 1640 medium supplemented with 10% heat-inactivated FBS. DG75 cells were transfected with 10 µg of pCIG CTSS^{WT} or CTSS^{Y132D} or pCIG Empty vector

(EV) together with respective HLA plasmid (10 μ g) using Gene Pulser II electroporation system (Bio-Rad). The following T cell clones recognizing different antigens of the Epstein-Barr virus were used in this study: the CD8⁺ T cell clones F#4 recognizing BZLF1 (aa₁₉₀₋₁₉₇ -RAKFKQLL-) on HLA-B*0801, and GLC#7 recognizing BMLF1 (aa₂₅₉₋₂₆₇ -GLCTLVAML-) on HLA-A*0201, as well as the CD4⁺ T cell clones 3#1 recognizing EBNA-LP (aa₄₃₋₅₅ -RRVRRRLVQEE-) on HLA-DPB1*1301, 3H11 recognizing BZLF1 (aa₁₇₄₋₁₈₈ -ELEIKRYKNRVASRK-) on HLA-DRB1*1301, #P11 recognizing BMLF1 (antigen aa-sequence unknown) on HLA-DRB1*1301, GBW3#5 recognizing BHRF1 (aa₁₆₁₋₁₇₅ -SRRFSWTLFLAGLTL-) on HLA-DPB1*0401, and HDe recognizing BBLF1 (aa₂₂₋₃₆ -GGIINLYNDYEEFN-) on HLA-DQB1*0501. The T cells were cultured in T cell media consisting of AIM-V (Invitrogen) medium supplemented with 10% heat-inactivated human serum, 2 mM L-glutamine, 1.25 μ g/mL fungizone, and 10 mM HEPES. For T cell stimulation, transfected DG75 cells were loaded with the indicated proteins at increasing concentrations for 4 hr, as described (Adhikary et al., 2007). Following wash out of unbound protein, 5×10^4 cells were mixed with 1×10^5 CD4⁺ T cells and co-cultured for 20 hr. IFN- γ secretion by the T cells was measured by ELISA (Mabtech). Pooling of these results is usually not done as T cells for different experiments are often derived from different donors at different time points, and the results in different experiments can differ substantially.

CTSS epitope prediction

NetMHC 4.0 software (<http://www.cbs.dtu.dk/services/NetMHC/>) was used to predict T cell epitopes within CTSS potentially binding to 12 supertype representative HLA-A and HLA-B alleles. Epitope prediction for HLA class II (NetMHCII 2.3) was performed to identify potential T cell epitopes within CTSS^{WT} and CTSS^{Y132D}.

Tumor inoculation and animal studies

BALB/c mice (N = 2) were injected with 5×10^6 sheep red blood cells (SRBCs) in PBS in lateral tail vein 10 days before isolation of their spleens and preparation of splenocyte suspensions as previously described (Yam and Hajjar, 2013).

A20 tumor cells (group I: 1×10^6 and group II: 1×10^5) were mixed 5:1 with splenocytes (group I: 0.2×10^6 and group: II 0.2×10^5) and cell mixtures were resuspended in PBS with 20% Matrigel and injected subcutaneously into the right flank. Group I consisted of N = 6 mice per cohort (EV versus CTSS^{hi} versus CTSS^{Y132D}), group II of N = 3 mice per cohort, respectively. Once tumors were visible, tumor sizes were measured every 2 - 3 days (volume = (length \times width²)/2). Mice were sacrificed when tumor volumes were > 500 mm³ or after a maximum of 21 days in group I. In group II all mice were sacrificed at day 18 regardless of their tumor size. The investigator was blinded to group allocation during the experiment and when assessing outcome.

Tumor isolation

After sacrificing the mice, tumors were isolated. A tumor piece was fixed in 10% formalin for 48 hr and then transferred to 70% ethanol for IHC staining. Single cell suspensions were prepared using the gentleMACS dissociator. Cells were counted and one vial of single cell suspension was frozen in 10% DMSO-FBS for flow-cytometry, another vial was snap frozen for Luminex analysis (see below).

Flow cytometry

The homogenized tumors samples were thawed and the cells were counted using Trypan Blue Solution 0.4% (GIBCO) with a hemocytometer. At minimum of 200000 viable cells were resuspended in 1 \times DPBS (GIBCO) and viable cells stained with ZombieUV Fixable Viability Kit (BioLegend) according to the manufacturer guidelines. Meanwhile, CD16/CD32 were blocked using Mouse BD FcBlock (BD Biosciences). Then, the extracellular markers were applied in a 100 μ L antibody mix solution with MACs Buffer (Miltenyi Biotec) for 15 min at RT. Finally, the samples were fixed with PBS-FA 1% and analyzed in a Cytotflex LX Flow cytometer (Beckman Coulter) where at least 10000 viable cells were recorded. Data analysis was performed in FlowJo v10 software using the area parameter in all the filters.

To identify the immune population infiltrates in the tumors, the following antibodies (eBioscience - ThermoFisher Scientific) were used: CD19 (clone #eBio1D3) conjugated to eFluor660, NK1.1 (clone #PK136) conjugated to Phycoerythrin (PE), TCR β (clone #H57-597) conjugated to Alexa Fluor (AF) 700, CD4 (clone #RM4-5) conjugated to Peridinin Chlorophyll Protein Complex (PerCP)-Cyanine (Cy) 5.5, and CD8 α (clone #53-6.7) conjugated to Brilliant violet (Bv) 763.

Mouse tumor immune assay (Luminex®100/200 System)

10 mg of snap frozen mouse tumor pieces from group II were lysed with passive lysis buffer (PLB) and IFN- γ levels determined using a mouse specific Bio-Plex Pro Reagent Kit 5 (Bio-Rad). Overall protein levels were determined using a bovine serum albumin (BSA) standard curve and 100 μ g of each tumor lysate were finally used in the assay.

Immunohistochemistry (IHC)

Staining of human pretreatment biopsies was performed with an automatic IHC cell stainer (BondMax, Leica). CD4 content was evaluated by visual inspection and counting of positive cells among 100 cells within a neoplastic follicle. Vessel density was determined by counting all CD34-positive capillary structures in one field of view with 550 μ m diameter (corresponding to a 400x magnification).

The following antibodies were used for human specimen: CD4 1:25 (Novocastra), CD34 1:700 (Beckman-Coulter). For correlations of IHC with NanoString derived gene expression we corrected the expression for the cancer cell fraction (CCF) by dividing the NanoString count by (1-CCF).

Staining of formalin fixed *mouse* tumors from group II was performed with an automatic IHC cell stainer (BenchMark Ultra, Ventana). The following antibodies were used on mouse tumors: CD4 1:500 (Abcam), CD8a (CST), CD45R/B220 1:150 (ThermoFisher Scientific), Ki-67 1:200 (Cell Marque).

Multispectral imaging analysis (Vectra® Polaris System)

1.5 μm thick tissue slides from FFPE-blocks were prepared and incubated overnight in a drying oven at 50–55°C, followed by deparaffinization in xylene two times for 15 min. Slides were rehydrated using an ethanol gradient (5 min ethanol absolute, 5 min 96% ethanol, 5 min 70% ethanol) ending with distilled water. Rehydrated slides were incubated in 4% buffered formalin for 20 min at room temperature and wash slides 3 times in distilled water for 2 min. Finally, slides were washed 3 times with 0.05% Tween-20 TBS buffer for 2 min each. Staining was performed with the Opal™ 7 Tumor Infiltrating Lymphocyte Kit (Cat. #OP7TL1001KT) according to the manufacturer's standard protocol. The following 5 antibodies were applied: PDL2 1:50 (Cell Signaling), PD1 1:80 (Medac), PDL1 1:150 (DCS), CD4 1:200 (Sigma-Aldrich), CD8 1:300 (PerkinElmer). Pictures were taken using the quantitative slide scanner (PerkinElmer) with the Vectra Polaris 1.0.7 and Phenochart 1.0.8 software. Quantification was performed in the inForm 2.4.2 software.

Profiling of the immune microenvironment

Digital multiplexed gene expression profiling of formalin-fixed and paraffin-embedded biopsy specimens of the GLSG2000 cohort was performed as previously described (Hellmuth et al., 2018). RNA from formalin-fixed and paraffin-embedded samples was isolated using the ExpressArt FFPE Clear RNAREady kit (AmpTec) or the AllPrep FFPE (QIAGEN). RNA (300 ng) was assayed with the nCounter PanCancer Immune Profiling Panel (NanoString) according to the manufacturer's protocol. Normalization was performed by subtracting the mean + 2 standard deviations of negative control as a cut-off and adjustment for geometric mean of defined positive controls and defined housekeeper genes. Housekeeping gene normalization threshold was set at 0.1–10-fold for quality control purposes.

The cohort from Tobin et al. (2019) was previously analyzed for immune-effectors (CD137, CD4, CD7, CD8A, TNF α), immune-checkpoints (PD1, PDL1, PDL2, TIM3, LAG3, FOXP3) and macrophages (CD68). GAPDH, OAZ1, PGAM1, PGK1 were used as housekeeping controls. To determine the CTSS expression in this cohort we assayed the RNA (50 ng) with the 12 gene nCounter® Elements XT Reagents gene kit (NanoString) using the same housekeeping genes. Oligonucleotides for CTSS were designed by NanoString nDesign Gateway and derived from Integrated DNA Technologies (IDT). Gene expression data were normalized using default settings in the nSOLVER 4.0 software.

Computational methods for molecular dynamics

The crystal structure of C139A mutant, human pro-CTSS was downloaded from the Protein Data Bank (PDB code: 2C0Y) (Kaulmann et al., 2006). C139 and the missing residues 108–113 were constructed with the UCSF Chimera package and *modeler* (Pettersen et al., 2004; Sali and Blundell, 1993). In order to generate the CTSS^{Y132D} coordinates, a point mutation was introduced using the UCSF Chimera package (Pettersen et al., 2004). The ASP rotamer with the highest probability according to the Dunbrack library was used (Dunbrack, 2002). All amino acid residues with polar side chains were set up in their charged forms, based on the acidic conditions used for the conversion and activity assays. The catalytic nucleophile C139 was set up in its deprotonated anionic form (Erez et al., 2009). The ff14SB molecular mechanics (MM) force field was assigned for all residues (Maier et al., 2015). CF counterions were added to neutralize the systems. Each system was placed into a pre-equilibrated OPC3 truncated octahedral water box (Izadi and Onufriev, 2016). The crystallographic water molecules were included into the solvent boxes which extended at least 9 Å from the solute atoms. The force field parameters and cysteine disulphide bonds were set up using the *leap* program of the AmberTools17 package. The equilibration of the systems and MD simulations followed a protocol published earlier (Bararia et al., 2016). An additional 10 ns MD simulation with no restraints was run in the isothermic-isobaric (NPT) ensemble in order to further equilibrate the systems. Production MD simulations were run for 100 ns and were carried out with the GPU accelerated version of the AMBER12 *pmemd* code (Götz et al., 2012; Salomon-Ferrer et al., 2013) on a Bull Cluster at the Center for Information Services and High Performance Computing (ZIH) at Technische Universität Dresden.

LC-MS/MS data acquisition

Peptides generated by in-gel trypsin digestion were dried in a vacuum concentrator and dissolved in 20 μL 0.1% formic acid (FA). LC-MS/MS measurements were performed on an Ultimate 3000 RSLCnano system coupled to a Q-Exactive HF-X mass spectrometer (ThermoFisher Scientific). For each analysis, 5 μL of peptides was delivered to a trap column (ReproSil-pur C18-AQ, 5 μm , Dr. Maisch, 20 mm \times 75 μm , self-packed) at a flow rate of 5 $\mu\text{L}/\text{min}$ in 100% solvent A (0.1% formic acid in HPLC grade water). After 10 min of loading, peptides were transferred to an analytical column (ReproSil Gold C18-AQ, 3 μm , Dr. Maisch, 400 mm \times 75 μm , self-packed) and separated using a 50 min gradient from 4% to 32% of solvent B (0.1% formic acid in acetonitrile and 5% (v/v) DMSO) at 300 nL/min flow rate. Both nanoLC solvents contained 5% (v/v) DMSO to boost the nanoESI response of peptides.

The Q-Exactive HF-X mass spectrometer was operated in data dependent acquisition and positive ionization mode. MS1 spectra (360–1300 m/z) were recorded at a resolution of 60,000 using an automatic gain control (AGC) target value of 3e6 and maximum injection time (maxIT) of 45 ms. After peptide fragmentation using higher energy collision induced dissociation (HCD), MS2 spectra of up to 18 precursor peptides were acquired at a resolution of 15,000 with an automatic gain control (AGC) target value of 1e5 and maximum injection time (maxIT) of 25 ms. The precursor isolation window width was set to 1.3 m/z and normalized collision energy to 26%. Dynamic exclusion was enabled with 25 s exclusion time (mass tolerance \pm 10 ppm).

LC-MS/MS database searching

Peptide identification and quantification was performed using MaxQuant (version 1.6.3.4) with its built-in search engine Andromeda (Cox et al., 2011; Tyanova et al., 2016). MS2 spectra were searched against the Flag-tagged Cathepsin S amino acid sequence supplemented with common contaminants (built-in option in MaxQuant). Carbamidomethylated cysteine was set as fixed modification and oxidation of methionine and N-terminal protein acetylation as variable modifications. Semi-specific Trypsin/P was specified as proteolytic enzyme. Precursor tolerance was set to 4.5 ppm, and fragment ion tolerance to 20 ppm. Results were adjusted to 1% false discovery rate (FDR) on peptide spectrum match (PSM) level employing a target-decoy approach using reversed protein sequences. The minimal peptide length was defined as 7 amino acids, the “match-between-run” function was disabled.

LC-MS/MS data analysis and visualization

Confident and reproducible CTSS peptide identification and quantification was ensured by filtering the peptide results table for peptides that were detectable in at least two replicates of at least one CTSS form. Additionally, also a peptide intensity filtering was performed, i.e., only CTSS peptides with a relative intensity $> 0.2\%$ in comparison to the most intense CTSS peptide in a specific sample were considered. In total 31 high confident CTSS peptides remained detectable over all 11 CTSS samples and could be mapped onto the primary sequence of CTSS.

CTSS copy number detection in patient samples

A total of 146 samples were used to generate genome wide copy number data with the Oncoscan FFPE CNV Assay (ThermoFisher Scientific). From these patients the cancer cell fraction of CTSS mutations was calculated using the genome-wide CNA data obtained by the Oncoscan Assay. The cancer cell fraction was generated using the Absolute algorithm as published elsewhere (Carter et al., 2012). Oncoscan CNV Assay was performed following the manufacturer’s instructions. Raw intensity (.CEL) files were read with Oncoscan Console and exported as normalized probe set intensities. All subsequent analysis including segmentation (minimal length for a segment was set to 10Kb) and log2 relative ratio (LRR) recentering were performed in R Studio 1.1.463 with R 3.6.0 using the libraries rCGH (1.14.0), DNACopy (1.58.0) and copy number (1.24.0). For 140 samples CTSS copy number gain information were inferred genome-wide from targeted NGS data utilizing both targeted reads as well as off-target reads (CNVkit 0.9.5) (Talevich et al., 2016). Validation of the segmented copy ratio values by CNVkit was performed with respect to Oncoscan. Depiction of patient samples with CTSS copy number gain and/or CTSS Y132D mutation was performed with the Oncoprint tool (Gao et al., 2013).

QUANTIFICATION AND STATISTICAL ANALYSIS

Statistical details of experiments can be found in the figure legends, where n represents the sample size or the number of biological replicates performed and N the population size. Pooled data are expressed as mean \pm SD, unless specified otherwise. For data excluding patient survival and POD24 analysis, GraphPad Prism 6 Version 1.2.1335 software was used to determine statistical significance using an unpaired Student’s t test compared to the control/untreated group, unless specified otherwise. A p value < 0.05 was considered as statistically significant.

For patient survival and POD24 analysis we only analyzed patients with advanced FL in need / receiving standard immunochemotherapy (R-CHOP or R-CVP or R-Bendamustine). Failure-free survival (FFS), overall survival, and POD24 were calculated as previously described (Jurinovic et al., 2016; Tobin et al., 2019). Patients were stratified by the presence of CTSS Y132D mutations (CTSS^{Y132D}), high CTSS expression (CTSS^{hi}), CTSS Y132D mutations or high CTSS expression (CTSS^{Y132D/hi}), and CTSS wild-type (WT) and not highly expressed (CTSS^{WT+low}). We used k-means clustering to identify cases with high versus low CTSS expression. Statistical analyses and data visualization were carried out with the statistical software R (version 3.6.0) using the packages survival 2.44.1.1, survminer 0.4.4, and ggplot2 3.2.0. Kaplan-Meier curves were compared using the log-rank test.

DATA AND CODE AVAILABILITY

Data referenced in this study are available in the Gene Expression Omnibus database with the accession codes GEO: GSE66166 and GEO: GSE62246. Additional gene expression data generated for this study is available at GEO with the accession code GEO: GSE147033 and GEO: GSE147125. Original data for all Figures have been deposited to Mendeley Data: <https://doi.org/10.17632/pr5cfx8mnh.1>.

The crystal structure of C139A mutant, human pro-CTSS is available at the Protein Data Bank (PDB: 2C0Y).

The mass spectrometry proteomics data have been deposited to the ProteomeXchange Consortium (<http://proteomecentral.proteomexchange.org>) via the PRIDE partner repository with the dataset identifier PRIDE: PXD014612).

DNA sequencing details on all CTSS mutations are provided in Table S3. Additional patient and sequencing data that support the findings of this study are available on request from the corresponding author (O.W.). The data are not publicly available as they contain information that could compromise research participant privacy or consent. Explicit consent to deposit raw-sequencing data was not obtained from the patients and samples were collected many years ago. Thus, the vast majority of patients cannot be asked to provide their consent.

The study did not generate previously unpublished custom code, software, or algorithm that is central to supporting the main claims.

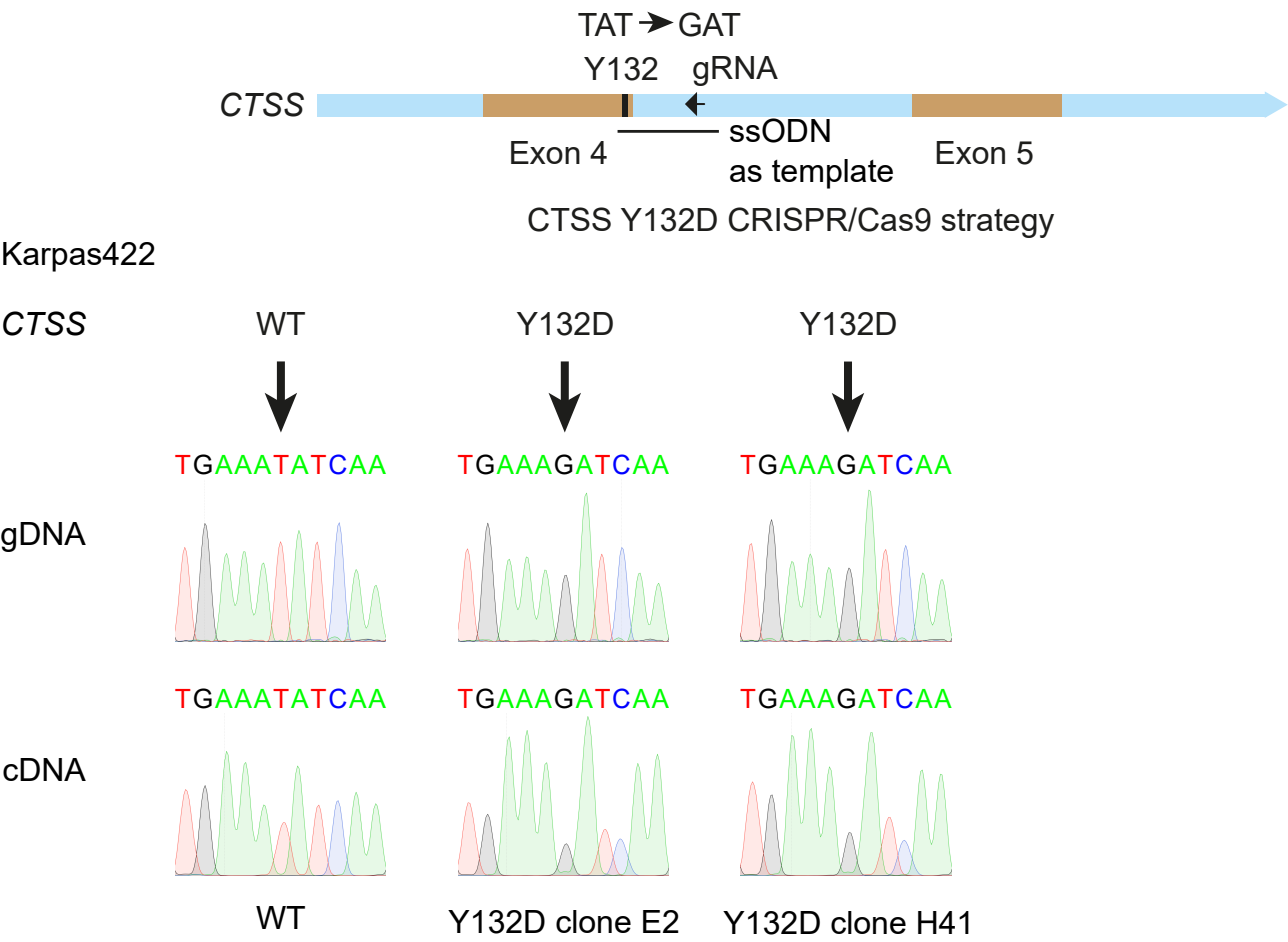
Supplemental Information

***Cathepsin S* Alterations Induce a Tumor-Promoting Immune Microenvironment in Follicular Lymphoma**

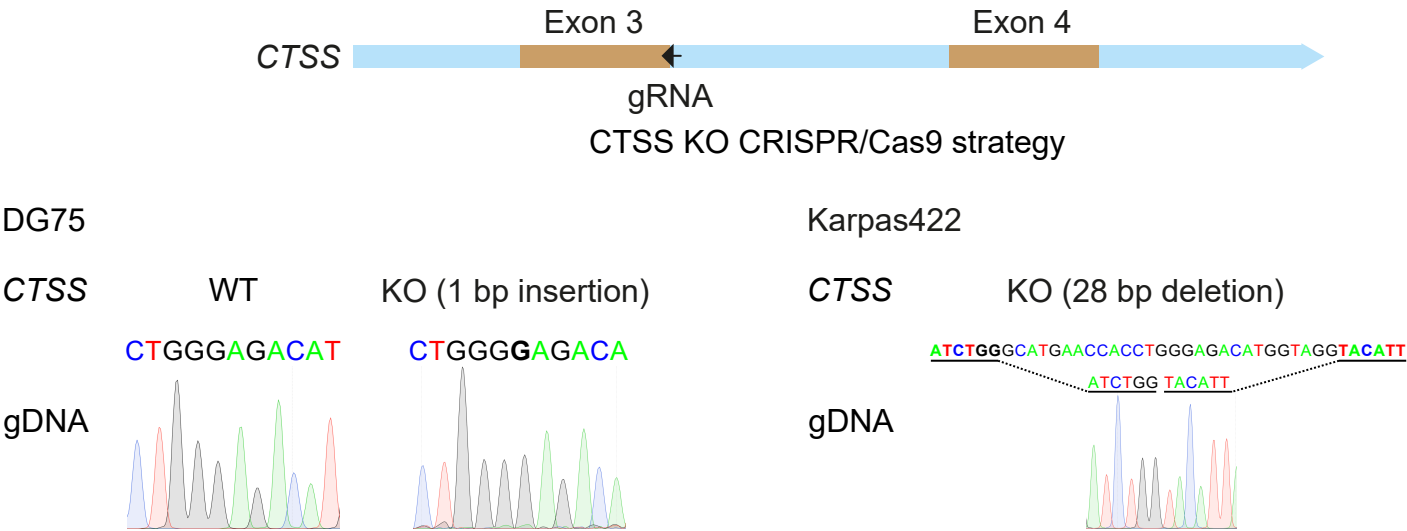
Deepak Bararia, Johannes A. Hildebrand, Sebastian Stolz, Sarah Haebe, Stefan Alig, Christopher P. Trevisani, Francisco Osorio-Barrios, Michael D. Bartoschek, Michael Mentz, Alessandro Pastore, Erik Gaitzsch, Michael Heide, Vindi Jurinovic, Katharina Rautter, Jay Gunawardana, Muhammed B. Sabdia, Monika Szczepanowski, Julia Richter, Wolfram Klapper, Abner Louissaint Jr., Christina Ludwig, Sebastian Bultmann, Heinrich Leonhardt, Sebastian Eustermann, Karl-Peter Hopfner, Wolfgang Hiddemann, Michael von Bergwelt-Baildon, Christian Steidl, Robert Kridel, Joshua W.D. Tobin, Maher K. Gandhi, David M. Weinstock, Marc Schmidt-Supprian, Menyhárt B. Sárosi, Martina Rudelius, Verena Passerini, Josef Mautner, and Oliver Weigert

Figure S1

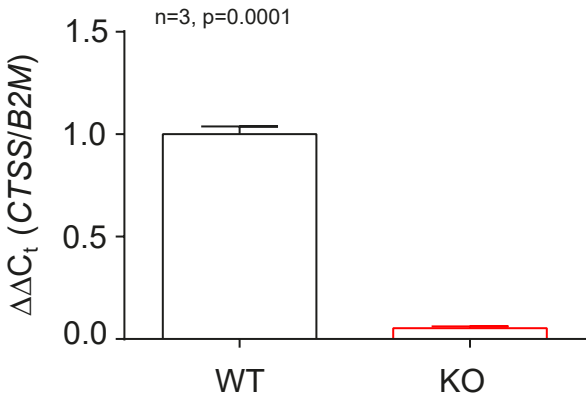
A



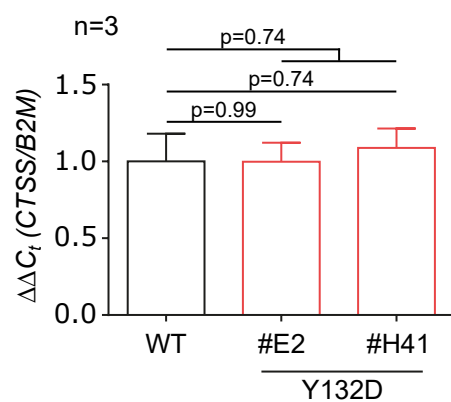
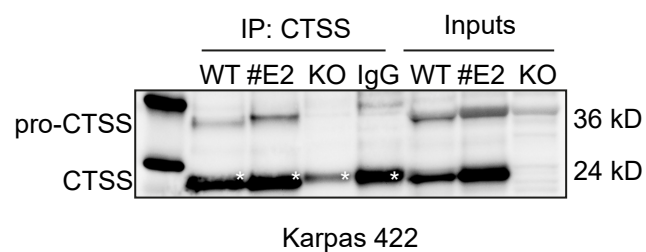
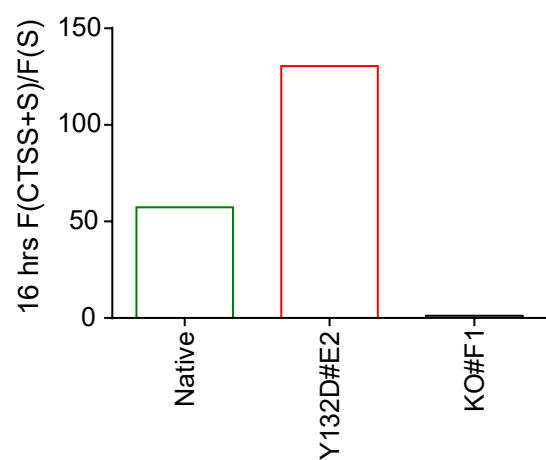
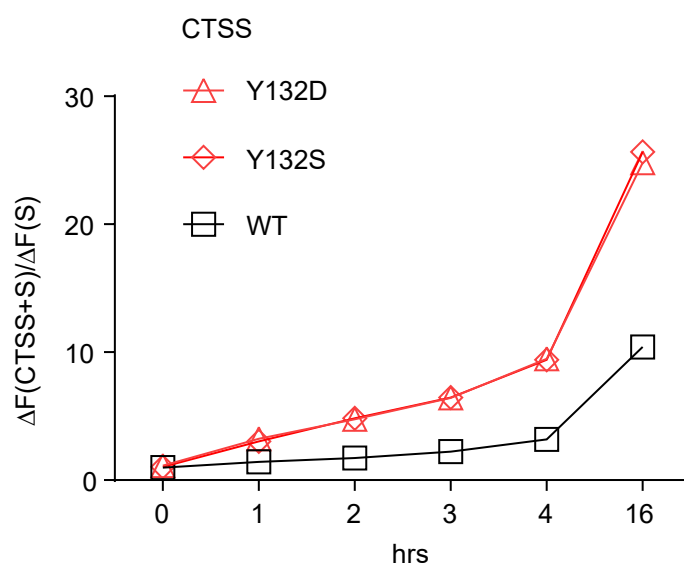
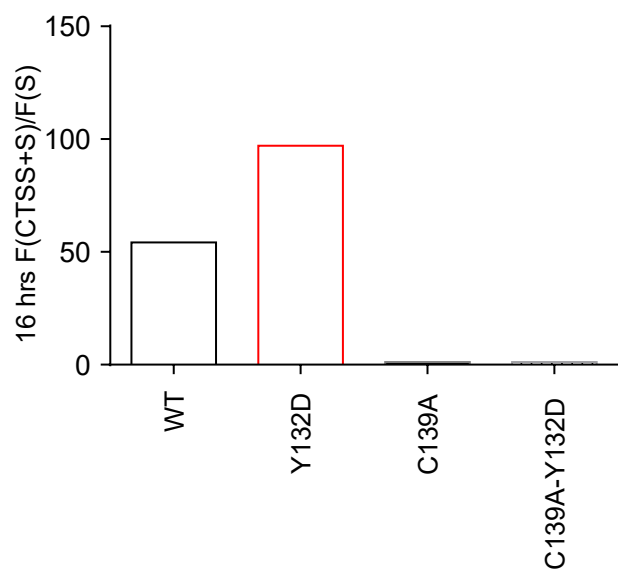
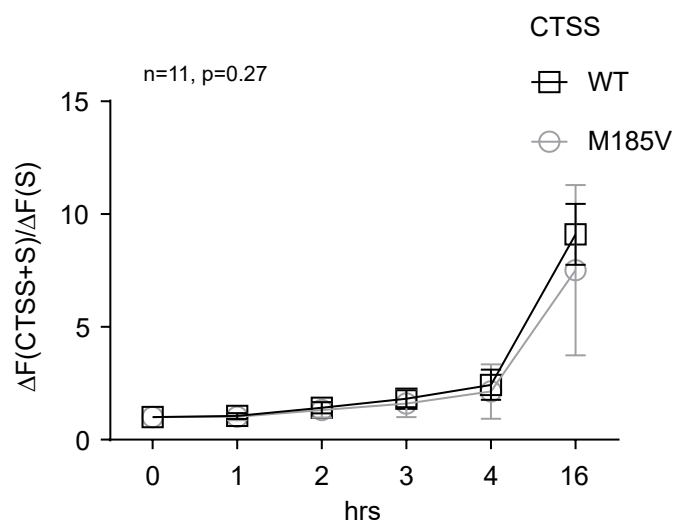
B



C



Supplementary Figure 1. CRISPR/Cas9 mediated *CTSS* Y132D knock-in and *CTSS* knock-out (KO) mutant cells. Related to Figure 2. **A)** Schematic overview of the target site in the *CTSS* locus showing Y132 in exon 4, the guided RNA binding orientation, and single stranded oligonucleotide donor (ssODN) as a template. Single base substitution (T to G) at the genomic (gDNA) and mRNA (c-DNA) levels were verified by Sanger sequencing. **B)** Schematic overview of the target site in the *CTSS* locus showing the position of the guided RNA for exon-intron boundary disruption. DG75 *CTSS*^{KO} (clone #2A1) has a single base insertion in exon 3 resulting in a frame-shift as detected by Sanger sequencing at the gDNA level. Karpas422 *CTSS*^{KO} clone (#F1) has a 28 bp deletion resulting in a non-functional protein. **C)** qRT-PCR for *CTSS* expression in DG75 native cells (*CTSS* WT) and in the DG75 *CTSS*^{KO} clone (#2A1). β -2 microglobulin (*B2M*) was used as a reference gene. Pooled data from biological replicates (N) are represented as mean \pm SD; p-values from unpaired Student's t test.

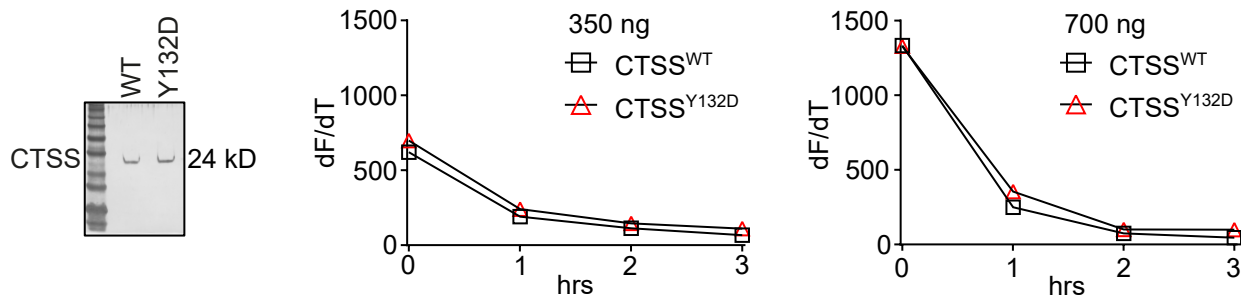
Figure S2**A****B****C****D****E****F**

Supplementary Figure 2. *In vitro* substrate cleavage activity from further CTSS mutants. Related to Figure 2.

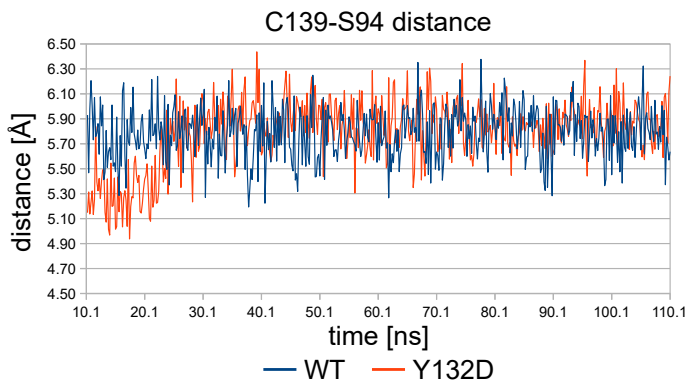
A) qRT-PCR of respective *CTSS* mRNA; $\Delta\Delta C_t$, difference (*CTSS* vs *B2M* reference gene). **B)** Western blot for CTSS immunoprecipitates (IP) from Karpas422 cells. Single cell derived Karpas422 *CTSS*^{KO} cells (clone #F1) were used as negative control. Asterisks indicate IgG light chains slightly above CTSS. **C)** CTSS substrate cleavage activity at 16 hours (hrs) with immunoprecipitates from B). F(CTSS)/F(S) is the fold-change after 16 hrs compared to AFC-signal without enzyme added (IP control). **D)** Substrate cleavage activity of immunoprecipitated CTSS Y132D and CTSS Y132S proteins from pCIG-*CTSS* (Y132D vs Y132S) transfected HEK293T cells. $\Delta F(CTSS)/\Delta F(S)$ is the fold-change over time compared to AFC-signal without enzyme added. **E)** CTSS substrate cleavage activity at 16 hours (hrs) with immunoprecipitated CTSS C139A and C139A-Y132D. F(CTSS)/F(S) is the fold-change after 16 hrs compared to AFC-signal without enzyme added (IP control). **F)** Substrate cleavage activity over time from N=11 biological replicates using immunoprecipitated CTSS M185V and CTSS WT from Karpas422 with or without CTSS M185V introduced by CRISPR/Cas9; data are represented as mean \pm SD; p-values from unpaired Student's t test.

Figure S3

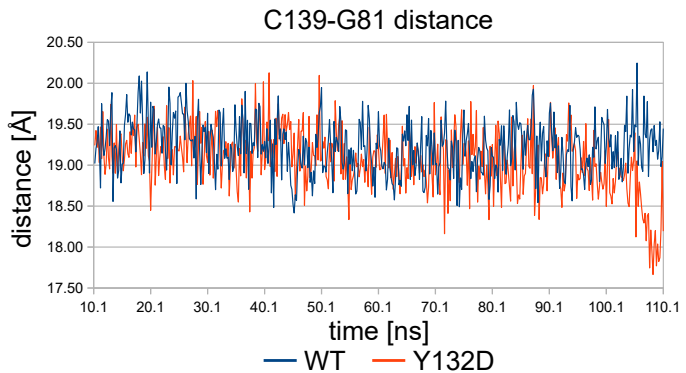
A



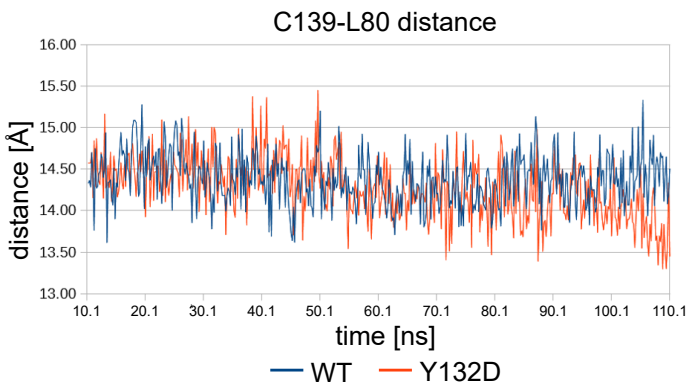
B



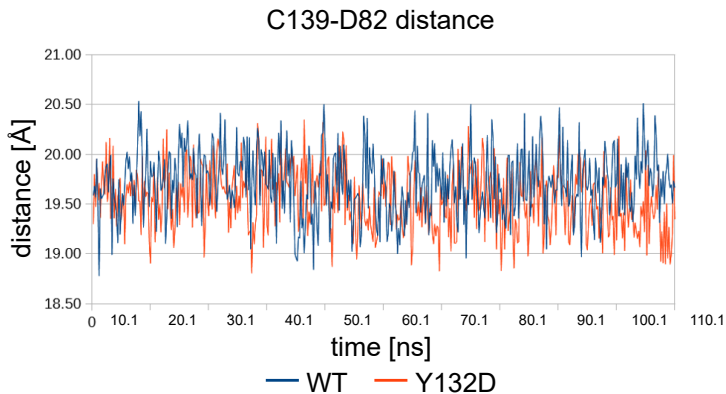
C



D



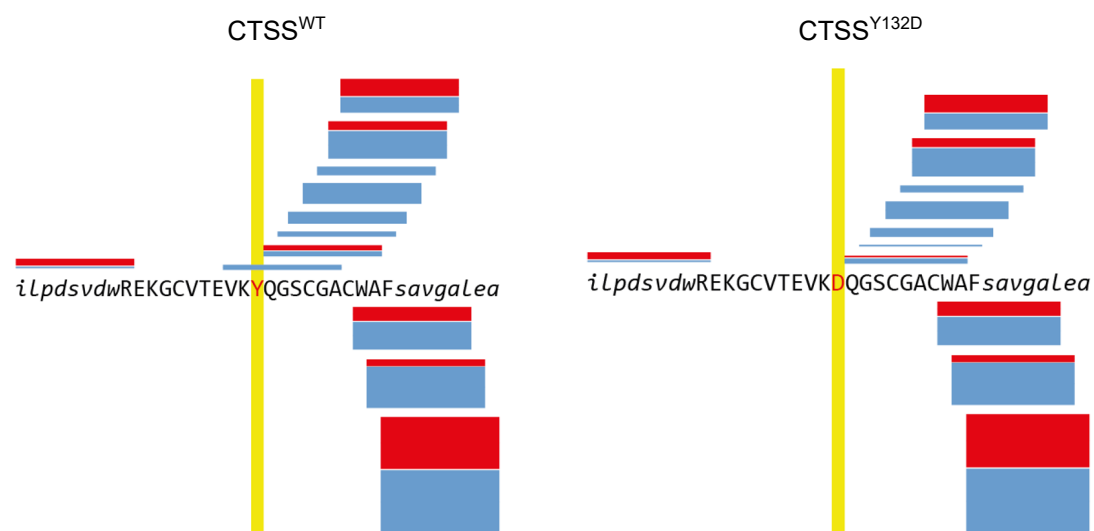
E



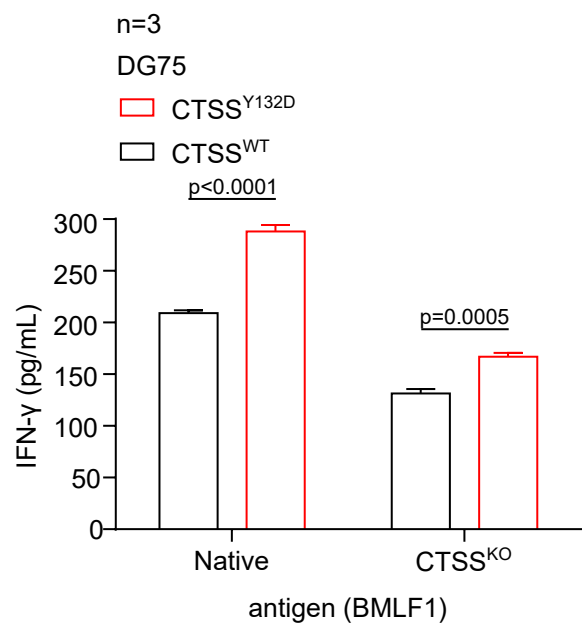
Supplementary Figure 3. Mature CTSS activity and structural modelling of CTSS WT vs CTSS Y132D. Related to Figure 3. A) CTSS substrate cleavage assay over 3 hrs using purified and completely converted mature CTSS (WT and Y132D), visualized in a silver stained gel. Two different starting concentrations are shown; dF/dt = rate of reaction. **B-E)** MD simulations of molecular distances between the center of mass of atoms: C139 and S94 (**B**), C139 and G81 (**C**), C139 and L80 (**D**), and C139 and D82 (**E**) (Y132D vs WT); Å = Ångström, ns = nanoseconds.

Figure S4

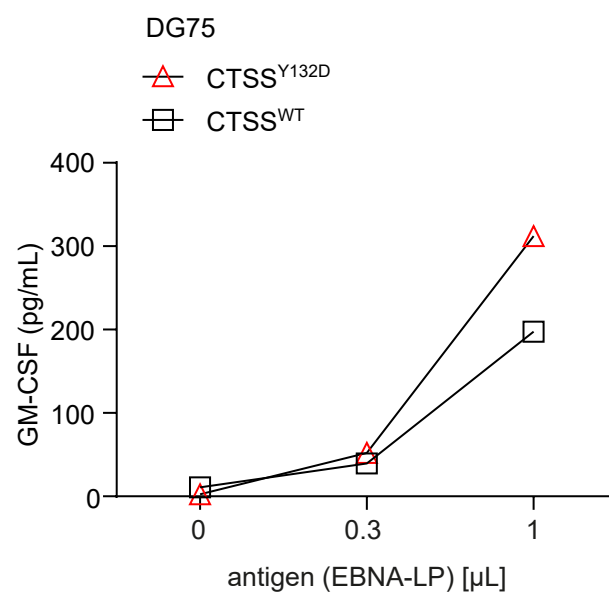
A



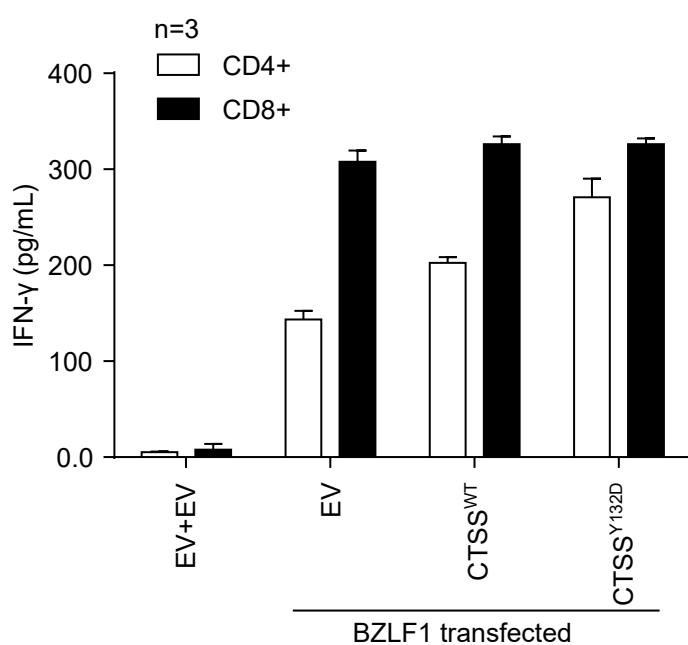
B



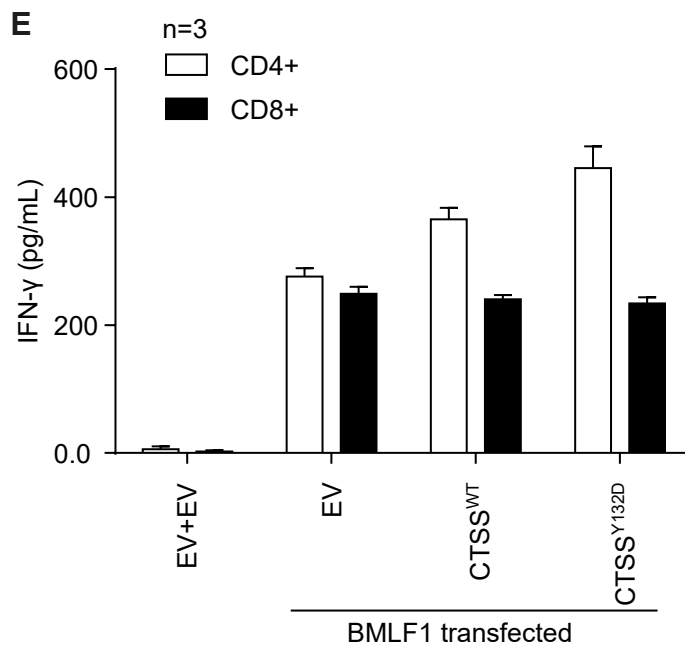
C



D



E

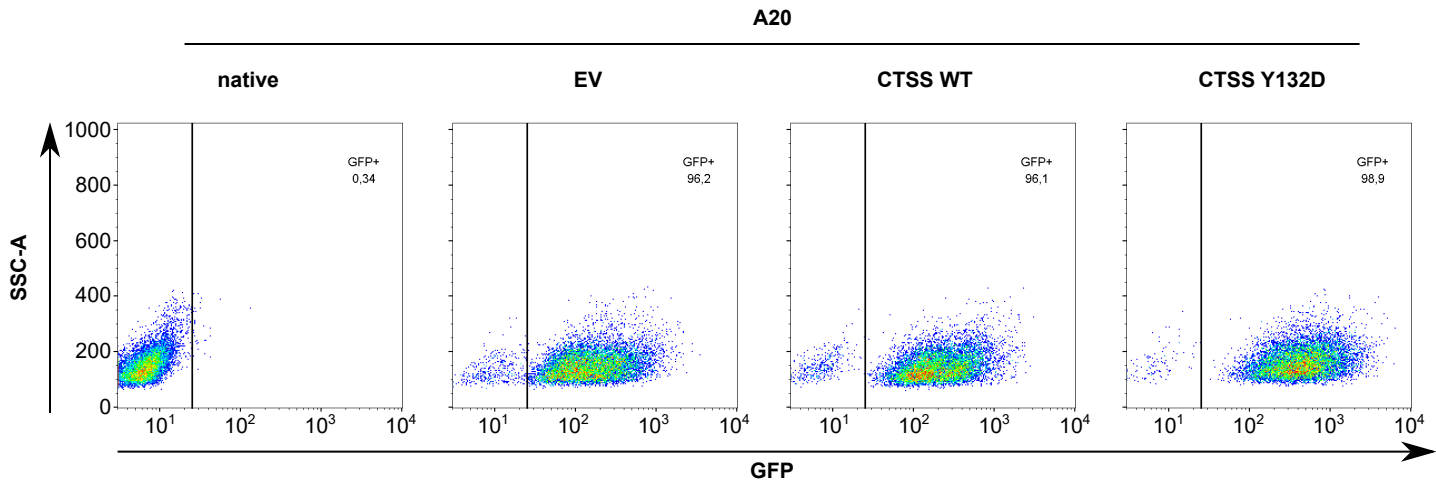


Supplementary Figure 4. CTSS Y132D and CTSS WT overexpression increase antigen-specific CD4⁺ but not CD8⁺ T-cell responses *in vitro*. Related to Figure 4. A) CD4⁺ T-cell epitope prediction (NetMHCII 2.3) within CTSS (WT vs Y132D) potentially binding to representative class II (25 HLA-DR, 20 HLA-DQ and 9 HLA-DP) alleles. Predicted epitopes are depicted as blue (predicted weak binders) or red (predicted strong binders) lines above and below the amino acid sequence of human CTSS. The thickness of the line represents the number of HLA alleles (1-37 alleles) to which the predicted epitope may bind. The position of amino acid 132 (Y) is marked in color, the adjacent 10 amino acids are in capital letters and the 8 N- and C-terminal flanking amino acids are shown in italics. **B)** DG75 native (*CTSS* WT) cells were transfected with *CTSS* WT (*CTSS*^{WT}) or Y132D (*CTSS*^{Y132D}) expression constructs along with MHC-II. Cells were incubated with increasing antigen concentrations (EBNA-LP) and co-cultured with antigen-specific CD4⁺ T-cells. GM-CSF in the supernatant was measured by ELISA. **C)** Similar to Figure 4G using BMLF-1 antigen. In this experiment, *CTSS* native and *CTSS*^{KO} cells were transfected in parallel. Data is representative of 3 independent experiments. **D)** DG75 native (*CTSS* WT) cells were transfected with *CTSS* WT (*CTSS*^{WT}) or Y132D (*CTSS*^{Y132D}) expression constructs along with BZLF1 and co-cultured with antigen-specific CD4⁺ and CD8⁺ T-cells in separate wells. Differences between CD8⁺ T-cell activation (black bars) are not significant. **E)** Similar to D) with BMLF1. Again, differences between CD8⁺ T-cell activation are not significant, $p > 0.6$ by 2-tailed Student's t-test.

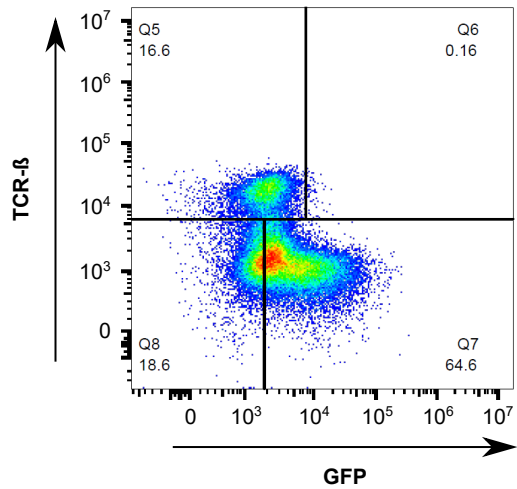
Pooled data from biological replicates (N) are represented as mean \pm SD; p-values from unpaired Student's t test.

Figure S5

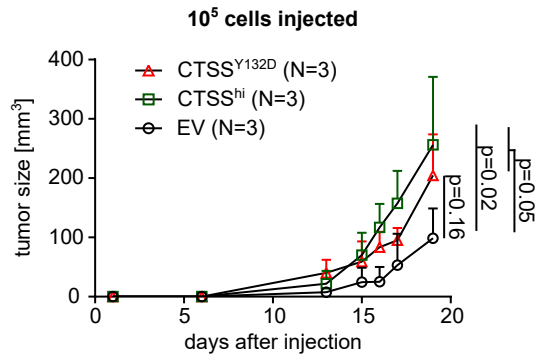
A



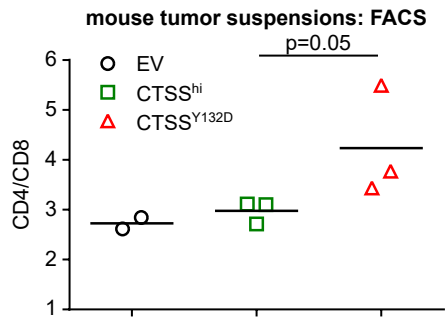
B



C



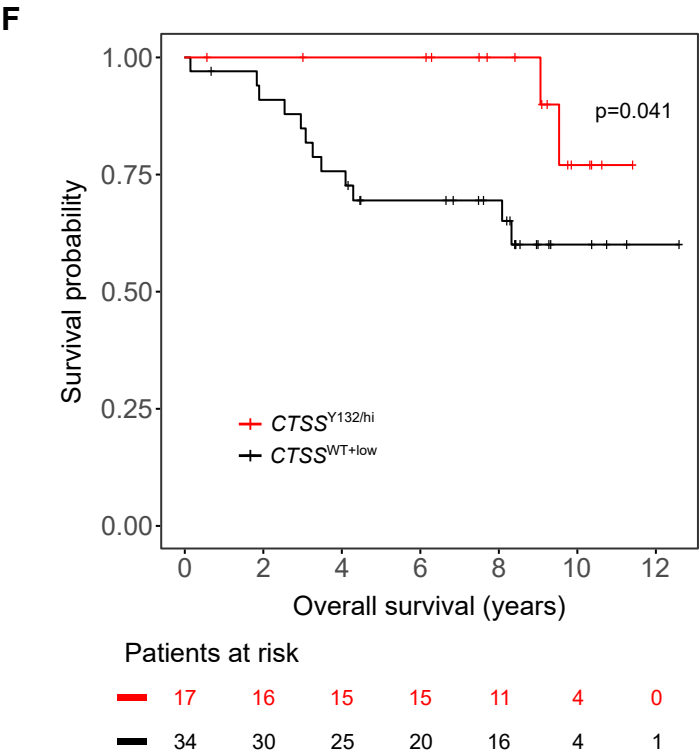
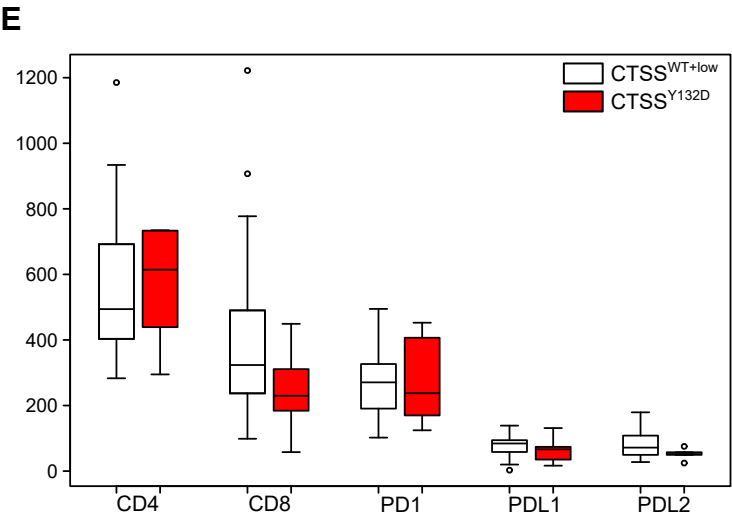
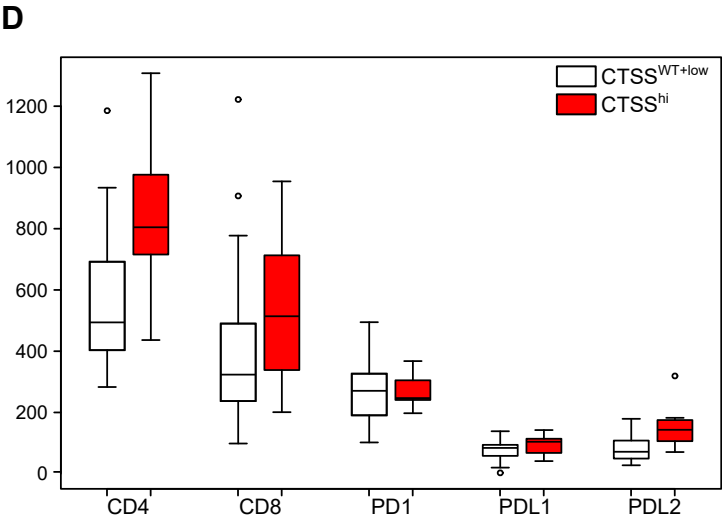
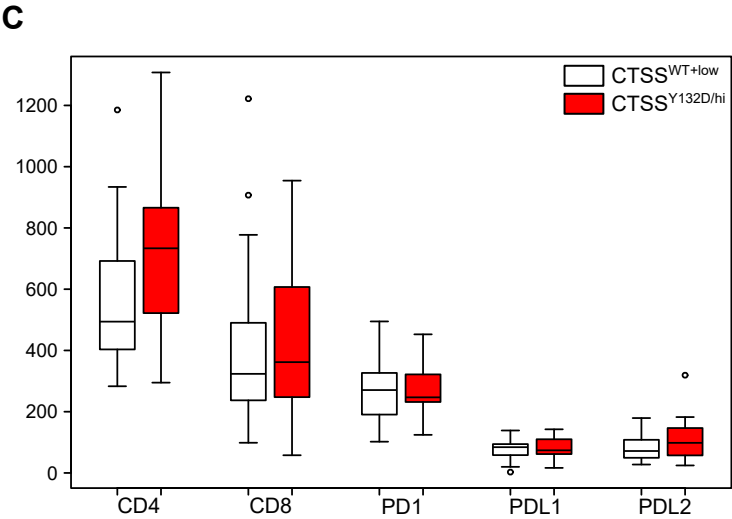
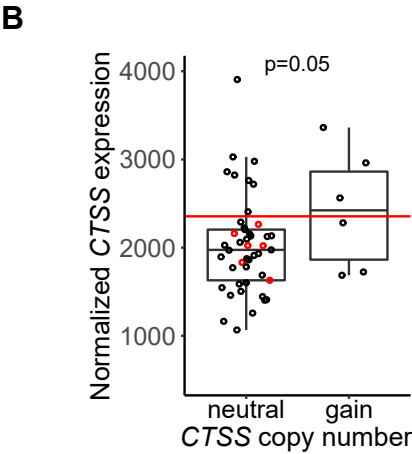
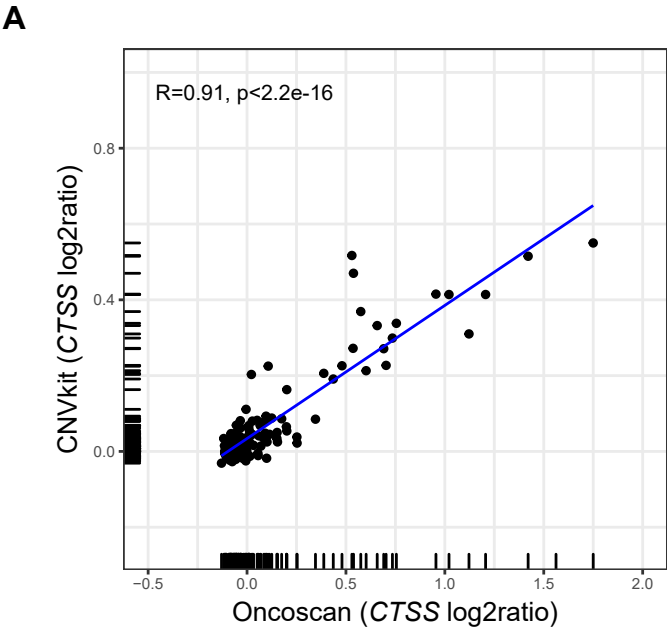
D



Supplementary Figure 5. Supplementary data for *in vivo* experiment. Related to Figure 5. **A)** FACS of native, empty vector (EV), *CTSS* WT and *CTSS* Y132D transduced A20 cells. **B)** FACS of a pre-injection mix consisting of splenocytes and transduced A20 cells in a 1 to 5 ratio. **C)** Tumor growth in BALB/c mice with N=3 mice per construct. Splenocytes (0.2×10^5) from sheep red blood cell (SRBC)-immunized BALB/c mice were mixed 1-to-5 with stably transduced A20 cells (1×10^5). 1.2×10^5 cells were then injected per BALB/c mouse (N=3 mice per group). **D)** FACS analysis of isolated tumor suspensions from C).

Pooled data from biological replicates (N) are represented as mean \pm SEM in C); p-values from unpaired Student's t test.

Figure S6

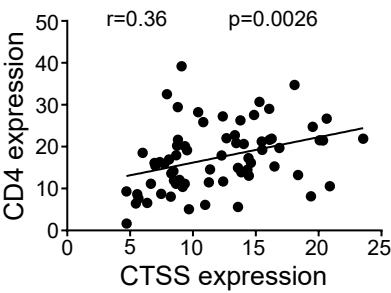


Supplementary Figure 6. CTSS hyperactivity in primary patient samples from the GLSG2000 cohort. Related

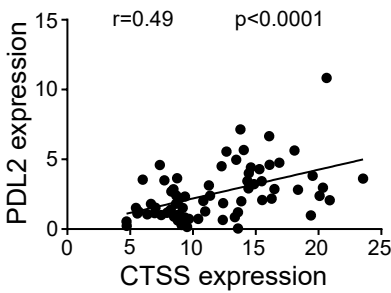
to Figure 6. A) Inferred copy number (CN) analysis from targeted DNA sequencing data. *CTSS* log2 values obtained from targeted DNA sequencing data and analyzed via the CNVkit pipeline plotted against the *CTSS* log2 values obtained from chromosome genomic array testing (CGAT, OncoScan) for a subset of our study cohort (N=146); Pearson's r and p-value are shown.. **B)** Normalized *CTSS* gene expression by *CTSS* CN status (neutral vs gain). Samples with high *CTSS* expression (above red line) were identified by k -mean clustering. FL with *CTSS* Y132 mutations are indicated by red circles; p-value from unpaired Student's t test. **C)** Boxplots comparing indicated immune genes in $CTSS^{WT+low}$ to $CTSS^{Y132D/hi}$ patients. **D)** Boxplots comparing indicated immune genes in $CTSS^{WT+low}$ to $CTSS^{hi}$ patients only. **E)** Boxplots comparing indicated immune genes in $CTSS^{WT+low}$ to $CTSS^{Y132D}$ patients only. The 50% quantile and the mean \pm SD are shown in C)-E). **F)** Kaplan-Meier plot for overall survival (OS) of patients with $CTSS^{Y132D/hi}$ FL (N=17) vs $CTSS^{WT+low}$ (N=34); p-value from log-rank test.

Figure S7

A

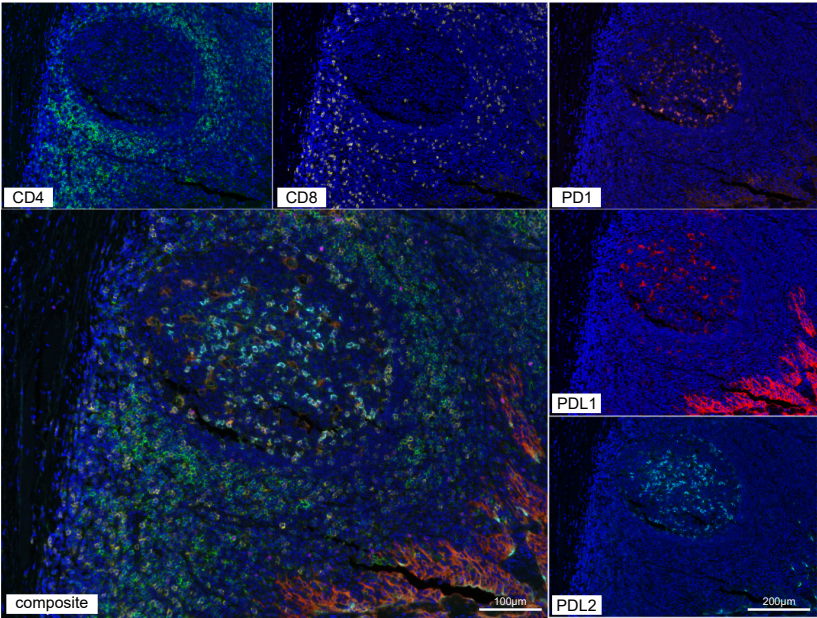


B



C

Tonsil



Supplementary Figure 7. CTSS hyperactivity in primary patient samples from independent validation cohort (Tobin et al., 2019). Related to Figure 7. A) Correlation of *CTSS* expression with *CD4* and **B)** *PDL2* expression. Pearson's *r* and *p*-value are shown. Data was generated with the Elements XT kit from NanoString. **C)** Multispectral imaging of a healthy human tonsil used as a control for staining patterns. Of note, CD4⁺ cells surround the germinal center.

Table S1. Oligonucleotides used for PCR, Sanger sequencing, CRISPR/Cas9 of CTSS. Related to STAR Methods.

Oligonucleotides		
CTSS_KO_sgRNA_Forward: CACCGtacctaccatgtctcccagg	This paper	N/A
CTSS_KO_sgRNA_Reverse: AAACcctgggagacatggttaggtac	This paper	N/A
CTSS_Y132D_repair template: agccagtggcagagaaatcacatataagtcaaaccctaatcggtattgcctgattct gtggactggagagagaaagggtgtgttactgaagtgaatGatcaagtgaattacca tccaagcGtctgaaccctaggtagagctctttaaagcttagtctagctacagaatttga cagtgaatcttacagtcccac	This paper	N/A
CTSS_Y132D_sgRNA_Forward: CACCGgagctctacctagggttcag	This paper	N/A
CTSS_Y132D_sgRNA_Reverse: AAACctgaaccctaggtagagctcC	This paper	N/A
Primer for PCR screening CTSS KO forward: AACACTTATTTGTCCAGGATGCAG	This paper	N/A
Primer for PCR screening CTSS KO reverse: TTCTGTACACGTTCTTACGTCCTT	This paper	N/A
Primer for PCR screening CTSS Y132D forward: GATGAGTTCCTGAGAGTTCCC	This paper	N/A
Primer for PCR screening CTSS Y132D reverse: ACACGTGGGACTGTAAGATTC	This paper	N/A
Primer for Sanger sequencing of plasmids CTSS forward: TGTGCTCTTGGTGTGCTCCT	This paper	N/A
Primer for Sanger sequencing of plasmids CTSS reverse: CATTGCAGCCTTTGTTTCCA	This paper	N/A
Primers to validate cDNA after CRISPR forward: CTGAGAGTTCCCAGCCAGTG	This paper	N/A
Primers to validate cDNA after CRISPR reverse: CAGGTTCTGGGCACTGAGAG	This paper	N/A

Table S2. Antibodies used for immunohistochemistry (IHC), flow cytometry (FACS) and immunoprecipitation (IP). Related to STAR Methods.

Table S2: Antibodies							
Purpose	ID	Company	Species	Clone	Dilution	Cat#	RRID
IHC on human tissue	CD34	Beckman-Coulter	mouse	QBEnd10	1:700	IM1185	AB_131602
	CD4	Leica Biosystems	mouse	4B12	1:25	PA0371	AB_1055443
	CTSS	R&D	goat	polyclonal	1:50	AF1183	AB_2087994
	CD8	DAKO	mouse	C8/144B	1:200	M7103,	AB_2075537
	PD1	CellMarque	mouse	MRQ-22	1:200	315M-95	AB_1160824
	PDL1	Cell Signaling	rabbit	E1L3N	1:200	13684	AB_2687655
IHC on mouse tumor tissue	CD4	abcam	rabbit	EPR19514	1:500	ab183685	AB_2686917
	CD45R/B220	BD	rat	RA3-6B2	1:200	553084	AB_394614
	ki67	Cell Marque	rabbit	SP6	1:200	275R-15	AB_1158033
Vectra Polaris on human tissue	PDL2	Cell Signaling	rabbit	D7U8C	1:50	82723	AB_2799999
	PD1	Medac	mouse	MRQ22	1:80	315M-95	AB_1160824
	PDL1	DCS	rabbit	QR1	1:150	PI516C002	N.A.
	CD4	Sigma-Aldrich	rabbit	EP204	1:200	104R-26	N.A.
	CD8	Cell Marque	mouse	C8/144B	1:300	108M-94	AB_1158205
FACS on mouse tumor suspensions	CD19 eFluor660	eBioscience	rat	eBio1D3	1:200	50-0193-82	AB_11218286
	NK1.1 PE	eBioscience	mouse	PK136	1:100	A26000	AB_2536060
	TCR β AF 700	eBioscience	hamster	H57-597	1:1500	56-5961-82	AB_2802349
	CD4 PerCP-Cy 5.5	eBioscience	rat	RM4-5	1:1000	45-0042-82	AB_1107001
	CD8 α Bv 763	eBioscience	rat	53-6.7	1:100	14-0081-82	AB_467087
Western blot	CD74	Abcam	mouse	2D1B3	1:1000	AB181465	N.A.
	CTSS (Peptide: Q17-I331)	R and D Systems	goat	polyclonal	1:2000	AF1183	AB_2087994
	FLAG-M2	Sigma-Aldrich	mouse	M2	1:5000	F3165	AB_259529
	Goat-IgG-HRP	Santa Cruz	donkey	polyclonal	1:2000	sc-2020	AB_631728
	HSP 90	Cell Signaling	rabbit	C45G5	1:5000	4877	AB_2233307
	Goat anti-Mouse IgG-HRP	Thermo Fisher	goat	Polyclonal	1:5000	31430	AB_228307
	Rabbit-IgG-HRP	Thermo Fisher	goat	polyclonal	1:2000	31460	AB_228341
	β -tubulin	Cell Signaling	rabbit	9F3	1:5000	2128	AB_823664
IP	Normal Goat IgG Control	R and D Systems	goat	polyclonal	1:200	AB-108-C	AB_35426
	CTSS (Peptide: Q17-I331)	R and D Systems	goat	polyclonal	1:100	AF1183	AB_2087994

Table S3. DNA sequencing details of CTSS mutations.

Gene	Patient ID	Type	Effect	Amino acid change	Reference base	Alternate base	Coverage	VAF	Cohort	Reported in
CTSS	1607	SNP	Missense	Y132D	A	C	293	0.38	GLSG	Pastore et al. 2015
CTSS	1653	SNP	Missense	Y132D	A	C	349	0.44	GLSG	Pastore et al. 2015
CTSS	1812	SNP	Missense	Y132D	A	C	278	0.22	GLSG	Pastore et al. 2015
CTSS	1890	SNP	Missense	M185V	T	C	180	0.31	GLSG	Pastore et al. 2015
CTSS	2025	SNP	Missense	Y132S	T	G	366	0.16	GLSG	Pastore et al. 2015
CTSS	2085	SNP	Missense	Y132N	A	T	128	0.08	GLSG	Pastore et al. 2015
CTSS	2209	SNP	Missense	G251A	C	G	311	0.36	GLSG	Pastore et al. 2015
CTSS	2223	SNP	Missense	Y132D	A	C	81	0.38	GLSG	Pastore et al. 2015
CTSS	2567	SNP	Missense	Y132D	A	C	199	0.07	GLSG	Pastore et al. 2015
CTSS	2659	SNP	Missense	Y132D	A	C	247	0.12	GLSG	Pastore et al. 2015
CTSS	2676	SNP	Missense	Y132N	A	T	172	0.07	GLSG	Pastore et al. 2015
CTSS	2772	SNP	Missense	Y132D	A	C	181	0.12	GLSG	Pastore et al. 2015
CTSS	2803	SNP	Missense	Y132D	A	C	212	0.12	GLSG	Pastore et al. 2015
CTSS	3018	SNP	Missense	Y132D	A	C	403	0.40	GLSG	Pastore et al. 2015
CTSS	3145	SNP	Missense	Y132D	A	C	93	0.27	GLSG	Pastore et al. 2015
CTSS	3175	SNP	Missense	Y132D	A	C	228	0.22	GLSG	Pastore et al. 2015
CTSS	3421	SNP	Missense	Y132D	A	C	92	0.23	GLSG	Pastore et al. 2015
CTSS	RG100	SNP	Missense	L80V	G	C	74	0.76	BCCA	Pastore et al. 2015
CTSS	RG136	SNP	Missense	Y267D	A	C	137	0.20	BCCA	Pastore et al. 2015
CTSS	RG62	SNP	Missense	Y132D	A	C	95	0.09	BCCA	Pastore et al. 2015
CTSS	RG64	SNP	Missense	Y132D	A	C	81	0.19	BCCA	Pastore et al. 2015
CTSS	RG76	SNP	Missense	Y132D	A	C	203	0.05	BCCA	Pastore et al. 2015
CTSS	24	SNP	Missense	Y132D	A	C	364	0.11	PAH	Tobin et al. 2019
CTSS	65	SNP	Missense	Y132D	A	C	884	0.22	PAH	Tobin et al. 2019
CTSS	124	SNP	Missense	Y132D	A	C	340	0.19	PAH	Tobin et al. 2019
CTSS	130	SNP	Missense	Y132D	A	C	297	0.15	PAH	Tobin et al. 2019
CTSS	188	SNP	Missense	Y132D	A	C	514	0.18	PAH	Tobin et al. 2019
CTSS	207	SNP	Missense	M185V	T	C	515	0.32	PAH	Tobin et al. 2019

SNP = Single Nucleotide Polymorphism, VAF = Variant Allele Frequency, GLSG = German Low-Grade Lymphoma Study Group, BCCA = British Columbia Cancer Agency, PAH = Princess Alexandra Hospital